

Review

A critical review of the pseudopotential multiphase lattice Boltzmann model: Methods and applications

Li Chen ^{a,b}, Qinjun Kang ^{b,*}, Yutong Mu ^a, Ya-Ling He ^a, Wen-Quan Tao ^a^aKey Laboratory of Thermo-Fluid Science and Engineering of MOE, School of Energy and Power Engineering, Xi'an Jiaotong University, Xi'an, Shaanxi 710049, China^bComputational Earth Science Group (EES-16), Los Alamos National Laboratory, Los Alamos, NM, USA

ARTICLE INFO

Article history:

Received 20 September 2013

Received in revised form 4 March 2014

Accepted 15 April 2014

Available online 15 May 2014

Keywords:

Pseudopotential model

Lattice Boltzmann method

Multiphase flow

Porous media

Slip phenomenon

Multiple physicochemical processes

ABSTRACT

This article presents a critical review of the theory and applications of a multiphase model in the community of the lattice Boltzmann method (LBM), the pseudopotential model proposed by Shan and Chen (1993) [4], which has been successfully applied to a wide range of multiphase flow problems during the past two decades. The first part of the review begins with a description of the LBM and the original pseudopotential model. The distinct features and the limitations of the original model are described in detail. Then various enhancements necessary to improve the pseudopotential model in terms of decreasing the spurious currents, obtaining high density/viscosity ratio, reducing thermodynamic inconsistency, unraveling the coupling between surface tension and equations of state (EOS), and unraveling the coupling between viscosity and surface tension, are reviewed. Then the fluid–solid interactions are presented and schemes to obtain different contact angles are discussed. The final section of this part focuses on the multi-component multiphase pseudopotential model. The second part of this review describes fruitful applications of this model to various multiphase flows. Coupling of this model with other models for more complicated multiple physicochemical processes are also introduced in this part.

© 2014 Elsevier Ltd. All rights reserved.

Contents

1. Introduction	211
2. The lattice Boltzmann method	212
3. The original Shan and Chen pseudopotential model	212
3.1. The original pseudopotential model	212
3.2. The limitations	213
3.2.1. The spurious current	213
3.2.2. The thermodynamic inconsistency	213
3.2.3. The limited density and viscosity ratios	214
3.2.4. The coupling between some properties	214
4. Improvements of the pseudopotential model	215
4.1. Incorporation of various equations of state	215
4.1.1. Yuan and Schaefer's method	215
4.1.2. Zhang and Tian's method	216
4.2. Calculation of the interaction force	216
4.2.1. Interaction force with high order isotropy	216
4.2.2. Midrange attractive interactions	217
4.2.3. Middle-range repulsion force	218
4.3. Force schemes	219
4.3.1. Velocity shift force scheme	219

* Corresponding author. Tel.: +1 505 665 9663; fax: +1 505 665 8737.

E-mail addresses: lichenht@gmail.com (L. Chen), qkang@lanl.gov (Q. Kang), muyutong@stu.xjtu.edu.cn (Y. Mu), yalinghe@mail.xjtu.edu.cn (Y.-L. He), wqtao@mail.xjtu.edu.cn (W.-Q. Tao).

4.3.2. Exact difference method (EDM)	219
4.3.3. Guo's force scheme	219
5. Fluid–solid interaction: contact angle	220
6. Multi-component pseudopotential model	220
7. Applications	221
7.1. Droplet/bubbles behaviors and contact line movement	222
7.1.1. Droplet sliding on a solid surface	222
7.1.2. Impingement of liquid droplets onto a dry surface	223
7.1.3. Superhydrophobic surface	223
7.1.4. Highly controlled formation of droplets	223
7.1.5. Droplets suspended in another immiscible fluid	224
7.1.6. Bubble rising in a stagnant liquid under buoyancy force	224
7.2. Slippage phenomena	225
7.3. Multiphase flow in porous media	226
7.3.1. Viscous fingering	226
7.3.2. Relative permeability	226
7.3.3. Effective diffusivity	228
7.3.4. Multiphase flow in proton exchange membrane fuel cell	229
7.4. Coupling with other methods for complicated multiple physicochemical processes	230
7.4.1. Coupled with thermal LB model for phase change heat transfer	230
7.4.2. Coupled with particle suspension model for solid particle suspension	232
7.4.3. Coupled with mass transport model for multiphase reactive transport process	232
8. Conclusion and discussion	232
Conflict of interest	233
Acknowledgments	233
References	233

1. Introduction

Multiphase fluid flows are ubiquitous in natural, scientific and engineering systems. A multiphase system can contain the same component with different phases such as a liquid water and water vapor system; multiple components with large density ratios between different components such as a liquid water and air system; and multiple components with a small density contrast between different components such as a liquid water and oil system. Simulation of multiphase flows is a problem often encountered in scientific and industrial applications and has long been regarded as a challenging task. Microscopically, the interfacial behaviors of multiphase flows result from the interactions among the constituent molecules. While the conventional multiphase flow models such as Level-Set method and Volume of Fluid method have been successfully adopted for simulating and investigating certain multiphase systems, there is still a need for alternative approaches to understand the connection between the macroscopic phenomena and the underlying microscopic dynamics at a much more fundamental level. Microscopic numerical methods such as molecular dynamics are suitable for capturing the microscopic interactions. However, they are often too computationally demanding to be applied to macroscopic scales of engineering interest.

Since the late 80s of last century, the lattice Boltzmann method (LBM), a new mesoscopic method based on the discrete kinetic theory, has emerged as a powerful tool for the numerical simulations and investigations of a broad class of complex flows, including porous flows, thermal flows, reactive transport, turbulence flows, and multiphase flows [1]. The LBM can be considered as a mesoscopic method, occupying the middle ground between the microscopic molecular dynamics and macroscopic fluid dynamics. The main strength of the LBM is that it behaves like a solver for the conservation equations such as Navier–Stokes equation in the bulk flow yet its mesoscopic nature provides a viable way to include the microscopic dynamics at the fluid–fluid and fluid–solid interfaces.

Several multiphase models have been developed in the community of the LBM during the past twenty years. The first

model is the so-called Rothman–Keller (RK) LB model using color gradients to separate and model the interaction at the multiphase interfaces, which was proposed by Gunstensen et al. in 1991 [2], based on the lattice gas model proposed by Rothman and Keller [3]. The second one is the pseudopotential model proposed by Shan and Chen [4–7] in which a pseudopotential is introduced to account for the nonlocal particle interactions. Another model is the free energy model proposed by Swift et al. [8] in which phase effects are directly introduced into the collision process by considering a generalized equilibrium distribution function that includes a non-ideal pressure tensor term. There are also other LB multiphase models such as the one proposed by He et al. [9] in which a mean-field method was developed where a proper force term was derived for multiphase behavior.

This review focuses on the pseudopotential model proposed by Shan and Chen in 1993 [4–7]. For general reviews of the LBM one is referred to [1,10–12], for the LBM in geology one is referred to [13], for the LBM for complex flow one is referred to [14], for the LBM for microfluidics one is referred to [15]. The pseudopotential model, to the best of the authors' knowledge, is the most widely used LB multiphase model due to its simplicity and versatility. The basic idea is to represent the microscopic molecular interactions at the mesoscopic scale using a *pseudo-potential* (also often called effective mass) depending on the local density. With such interactions, a single component single fluid spontaneously segregates into two phases with high and low densities when the interaction strength (or the temperature) is under the critical point (The critical point is the point at which the phase boundary between liquid and gas terminates and above which distinct liquid and gas phases do not exist). Such automatic phase separation is an attractive characteristic of the pseudopotential model, as the phase interface is no longer a mathematical boundary and no explicit interface-tracking or interface-capturing technique is needed. The phase interface is a post-processed quantity that can be characterized through monitoring the variation of the fluid densities. The densities change smoothly from one bulk value to another across the phase interface which usually has the width of several lattice nodes. Despite its simplicity, the pseudopotential model captures the

essential elements of the non-ideal fluid behaviors, namely a non-ideal equation of state (EOS) and a surface tension force. Due to its remarkable computational efficiency and clear representation of the underlying microscopic physics, this model has been a promising technique for simulating and investigating multiphase flow problems, particularly for these flows with complex topological changes of the interface (deformation, coalescence, breakup, etc.) or in complicated geometries. It has been successfully applied to a broad range of sciences such as energy, environment, chemistry, biology and geology.

The present review is divided into two main parts. In the first part, the theory of the pseudopotential model and its recent improvements are introduced. We first review the single-component pseudopotential model for bulk flows without solid boundaries. The techniques of incorporating various EOS, calculating the interaction force and implementing the forces into the LB framework, as well as their effects on overcoming the limitation of the original pseudopotential model are presented and discussed in detail. We then review the fluid–solid interaction forces and the contact angle. Finally in the first part, we discuss the multi-component multiphase pseudopotential model. In the second part, the applications of the pseudopotential model to various problems, including droplet/bubble behaviors with/without contact with solid walls, slippage phenomenon, multiphase flow in porous media, and coupling with other models for complex multiple physicochemical processes are reviewed and discussed.

2. The lattice Boltzmann method

In recent years, LBM has emerged as a powerful alternative CFD (computational fluid dynamics) method for studying fluid flow and transport processes. The LBM is a mesoscopic method for the description of fluids. While it originated from the Cellular Automata models, it can also be considered as a discrete form of the Boltzmann's equation [16]. In the LB method, the motion of fluid is described by a set of particle distribution functions. Based on the simple and popular Bhatnagar–Gross–Krook (BGK) collision operator [17], the standard LB equation with a force term can be expressed as follows

$$\begin{aligned} & f_{\sigma,\alpha}(\mathbf{x} + \mathbf{c}\mathbf{e}_\alpha \Delta t, t + \Delta t) - f_{\sigma,\alpha}(\mathbf{x}, t) \\ &= -\frac{1}{\tau_{\sigma,v}}(f_{\sigma,\alpha}(\mathbf{x}, t) - f_{\sigma,\alpha}^{\text{eq}}(\mathbf{x}, t)) + F_{\sigma,\alpha}(\mathbf{x}, t) \end{aligned} \quad (1)$$

where $f_{\sigma,\alpha}(\mathbf{x}, t)$ is the density distribution function of the component σ at the lattice site \mathbf{x} and time t , f^{eq} is the equilibrium distribution function, $c = \Delta x / \Delta t$ is the lattice speed with Δx and Δt as the lattice spacing and time step (Both Δx and Δt equal 1 in the lattice system), respectively, and τ_v is the dimensionless relaxation time. The left-hand side (LHS) of Eq. (1) represents the streaming step whereas the right-hand side (RHS) stands for the collision operator which leads the system to the local Maxwellian equilibrium on a time scale τ . The discrete velocities \mathbf{e}_α depend on the particular velocity model, and the D2Q9 (two-dimensional nine velocity) square and D3Q19 (three-dimensional 19 velocity) cubic model are commonly adopted. In this review, without loss of generality, the discussion is focused on two-dimensional space with the D2Q9 lattice structure, as shown in Fig. 1. For the D2Q9 model, \mathbf{e}_α are given by

$$\mathbf{e}_\alpha = \begin{cases} 0 & \alpha = 0 \\ \left(\cos \left[\frac{(\alpha-1)\pi}{2} \right], \sin \left[\frac{(\alpha-1)\pi}{2} \right] \right) & \alpha = 1, 2, 3, 4 \\ \sqrt{2} \left(\cos \left[\frac{(\alpha-5)\pi}{2} + \frac{\pi}{4} \right], \sin \left[\frac{(\alpha-5)\pi}{2} + \frac{\pi}{4} \right] \right) & \alpha = 5, 6, 7, 8 \end{cases} \quad (2)$$

The equilibrium distribution functions f^{eq} for the D2Q9 lattice are of the form

$$f_{\sigma,\alpha}^{\text{eq}} = \omega_\alpha \rho_\sigma \left[1 + \frac{3}{c^2} (\mathbf{e}_\alpha \cdot \mathbf{u}) + \frac{9}{2c^4} (\mathbf{e}_\alpha \cdot \mathbf{u})^2 - \frac{3}{2c^2} \mathbf{u}^2 \right] \quad (3)$$

where the weight factors ω_α are given by $\omega_0 = 4/9$, $\omega_{1-4} = 1/9$, and $\omega_{5-8} = 1/36$. The fluid density ρ_σ and fluid velocity \mathbf{u}_σ can be obtained from the first and second moments of the density distribution functions

$$\rho_\sigma = \sum_\alpha f_{\sigma,\alpha} \quad (4)$$

$$\rho_\sigma \mathbf{u}_\sigma = \sum_\alpha f_{\sigma,\alpha} \mathbf{e}_\alpha \quad (5)$$

$$\text{The viscosity in the lattice unit is related to the relaxation time by } v_\sigma = c_s^2 (\tau_{\sigma,v} - 0.5) \Delta t \quad (6)$$

where c_s is the lattice sound speed.

3. The original Shan and Chen pseudopotential model

3.1. The original pseudopotential model

In order to introduce nonlocal interaction among particles, Shan and Chen [4,5] defined the force experienced by the particles of component σ at \mathbf{x} from the particles $\bar{\sigma}$ at \mathbf{x}' as the following form

$$\mathbf{F}(\mathbf{x}, \mathbf{x}') = -G(|\mathbf{x} - \mathbf{x}'|) \psi_\sigma(\mathbf{x}) \psi_{\bar{\sigma}}(\mathbf{x}') (\mathbf{x}' - \mathbf{x}) \quad (7)$$

where G is a Green's function and ψ is an effective mass depending on the local density. The components σ and $\bar{\sigma}$ can be different or the same. Here we first discuss the single-component system. After it is thoroughly discussed we then move to multi-component system. The structure of the force along the vector between two lattice locations given by Eq. (7) is delicately designed. It is perhaps the most general one that meets the Newton's third law and conserves momentum globally [18]. The force is basically pairwise point coupling between the effective mass at the location \mathbf{x} and that at the neighboring location \mathbf{x}' . This type of interaction force among the particles does not conserve the local momentum during the collision process because the force behaves as an external force acting on the site. However, it has been proved that the total momentum of the system is conserved and no net momentum is introduced into the system [5]. The total force acting on the particles at \mathbf{x} is thus the sum of all the interaction forces

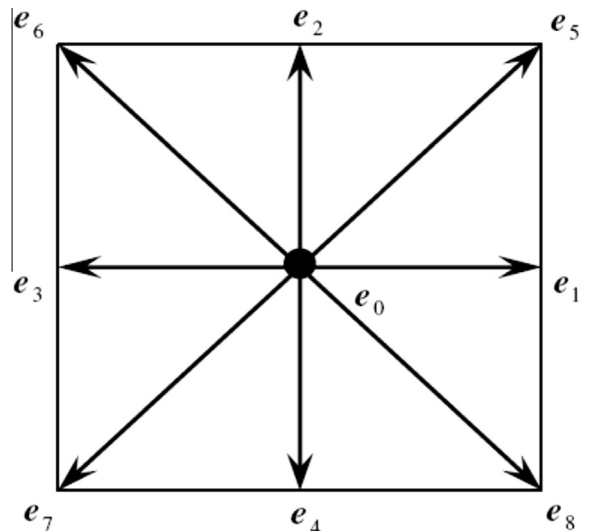


Fig. 1. Lattice structure and velocity vector of D2Q9 model.

$$\mathbf{F}(\mathbf{x}) = -\psi(\mathbf{x}) \sum G(|\mathbf{x} - \mathbf{x}'|) \psi(\mathbf{x}') (\mathbf{x}' - \mathbf{x}) \quad (8)$$

In the lattice space system, if we consider N neighbor sites that interact with the current site \mathbf{x} and let $G(|\mathbf{e}_z|)$ be a function of $|\mathbf{e}_z|$ only (which indicates that the interaction is isotropic), the interaction force can be further expressed as

$$\mathbf{F}(\mathbf{x}) = -g\psi(\mathbf{x})c_s^2 \sum_{z=1}^N w(|\mathbf{e}_z|^2) \psi(\mathbf{x} + \mathbf{e}_z) \mathbf{e}_z \quad (9)$$

where g is the interaction strength. $w(|\mathbf{e}_z|^2)$ are the weights used for the calculation of the isotropic interaction force, and it is different from that in Eq. (3).

There are three important elements in the force given by Eq. (9): the interaction strength g , the effective mass ψ , and the determination of the neighbor nodes. The g controls the interaction strength between particles, with a positive (negative) value leading to a repulsive (attractive) force between particles. The original form of effective mass in the work of Shan and Chen is [4,5]

$$\psi = \rho_0 \left(1 - \exp \left(-\frac{\rho}{\rho_0} \right) \right) \quad (10)$$

where ρ_0 is a normalization constant which is usually chosen as 1. This form of effective mass reduces to density ρ itself when ρ is low and reaches a saturation value at high density, as can be seen in Fig. 2. In Fig. 2, the EOS corresponding to Eq. (10) is named Shan-Chen EOS. The feature of approaching a saturation value at high density helps prevent density collapse of the phase with high density and thus can increase the simulation stabilities [19,20]. Besides, such an effective mass can produce an exponentially vanishing force as the density increases.

Through Taylor expansion, the leading terms of the interaction force expressed by Eq. (9) can be obtained as follows [18]

$$\mathbf{F} = -g \left(c_s^2 \psi \nabla \psi + \frac{c_s^4}{2} \psi \nabla (\Delta \psi) + \dots \right) \quad (11)$$

Despite its simplicity, with this force in the LB model two major ingredients of non-ideal fluids are captured, namely, a non-ideal EOS relating to the first term and the surface tension relating to the second term on RHS of Eq. (11). The correction to the ideal EOS $p = \rho c_s^2$ due to the introduction of this force leads to the following non-ideal EOS [4,5]

$$p = \rho c_s^2 + \frac{g}{2} c_s^2 \psi^2 \quad (12)$$

The distinct characteristics of the original pseudopotential model include the explicitly introduced interaction force, the effective mass with the form given by Eq. (10), the nearest and next-nearest

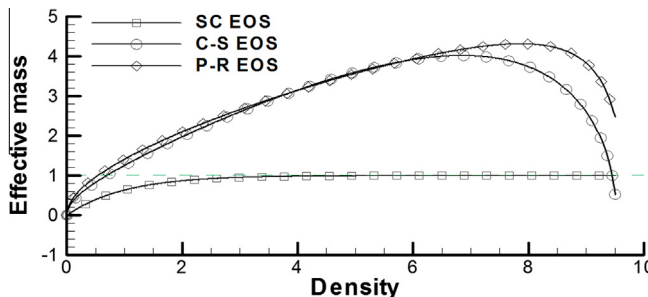


Fig. 2. The relationship between density and effective mass for the SC EOS, C-S (Carnahan–Starling) EOS and the P-R (Peng–Robinson) EOS. It can be seen that the effective mass of SC EOS achieves a saturation value as the density increases. The effective mass for the C-S EOS and P-R EOS, however, first increases to a peak value and then quickly decreases even to a negative value, which has no obvious physical meaning.

neighboring nodes adopted for calculating the interaction force, and the velocity shift force scheme (See Section 4.3) for incorporating the interaction force into the pseudopotential model. Hou et al. [21] compared this model with the RK LB multiphase model by simulating a static bubble in a fully periodic system and found that the pseudopotential model presents as a major improvement over the RK LB multiphase model.

Because of its computational efficiency and conceptual simplicity, the pseudopotential model has been widely employed for the simulations of a variety of multiphase flows. However, the original pseudopotential model suffers from some limitations which restrict its applications and incur criticisms on this model. Some of the limitations are inherent to this particular model and others are common problems shared by other multiphase flow models. These limitations include the relatively large spurious currents, thermodynamic inconsistency, the low density and kinematic viscosity ratios, the coupling between the EOS and surface tension, and the dependence of surface tension and density ratio on the viscosity (or the relaxation time). These limitations are introduced in detail as follows.

3.2. The limitations

3.2.1. The spurious current

The spurious current denotes the non-zero vortex-like fluid velocity in the vicinity of phase interface. It is also called artificial current or parasitic flow, and is a common problem for many multiphase flow models. The spurious current is commonly studied by simulating a static droplet (bubble) in a gravity-free fully periodic domain, as shown in Fig. 3. Physically, the droplet (bubble) and the surrounding gas (liquid) are at rest and the pressure difference inside and outside the droplet (bubble) should be balanced by the surface tension, as the Laplace law states. However, due to the limited discretization in calculating the corresponding gradient, the pressure difference and surface tension are not exactly balanced, leading to the artificial vortex-like velocity at the droplet (bubble) interface as shown in Fig. 3. The amplitude of the spurious currents increases as density ratio goes up, which causes the numerical instability and limits the maximum density ratios achievable. In addition to causing numerical instability (or divergence when spurious currents are strong), the spurious currents cannot be easily distinguished from the real flow velocities, thus casting doubt on the accuracy of the simulated flow field [22].

3.2.2. The thermodynamic inconsistency

Before discussing the thermodynamic inconsistency, we first introduce the Maxwell equal-area construction technique [23]. In thermodynamics, the densities of the vapor phase and liquid phase are determined by the system equilibrium. The Maxwell construction is adopted to obtain the vapor and liquid densities from a given $p-v$ curve. Fig. 4 shows an isotherm $p-v$ curve of a non-ideal gas described by C-S (Carnahan–Starling) EOS (the detail of the C-S EOS can be found in Section 4.1.1) at $T < T_c$ (T_c is the critical temperature). The basic idea of the Maxwell construction is that the area of two regions A (region123) and B (region345) should be equal, namely

$$\int_{v_1}^{v_v} p d\nu = p_s(v_v - v_1) \quad (13)$$

where p_s is the saturation pressure at a given temperature. It is obvious that if the EOS is known, the density of the liquid and vapor can be obtained by iteratively solving Eq. (13) at a given temperature.

For the pseudopotential model, the following relation is obtained [18]

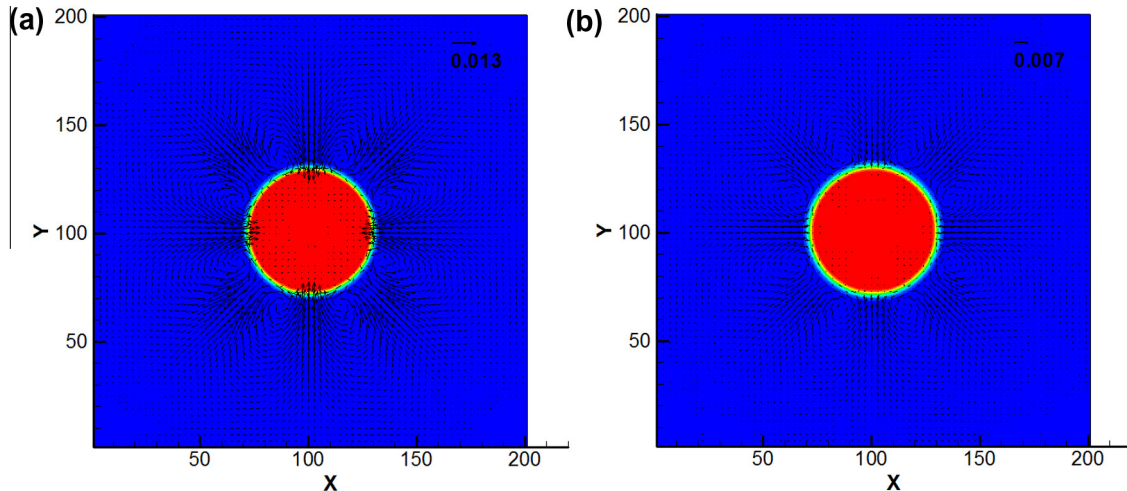


Fig. 3. Simulation results of a static circular liquid droplet embedded in a vapor phase in a gravity-free periodic field with different isotropic orders of the interaction force (a) isotropic order of 4, (b) isotropic order of 8. The simulation domain consists of 201×201 lattice nodes. The initial droplet radius is 30 lattices, and $T = 0.7T_c$. C-S EOS is used. The maximum spurious current decreased from 0.013 for isotropic order of 4 to 0.007 for isotropic order of 8.

$$\int_{\rho_v}^{\rho_1} \left(p_s - \rho c_s^2 - \frac{g}{2} c_s^2 \psi^2 \right) \frac{\psi'}{\psi} d\rho = 0 \quad (14)$$

where p_s is the saturation pressure and can be solved from Eq. (13). Eq. (14) is usually referred to mechanical stability condition. On the other hand, in the thermodynamics, the Maxwell equal-area construction requires that

$$\int_{\rho_v}^{\rho_1} \left(p_s - \rho c_s^2 - \frac{g}{2} c_s^2 \psi^2 \right) \frac{1}{\rho^2} d\rho = 0 \quad (15)$$

Here Eq. (12) has been used to derive Eq. (15). Comparing Eq. (14) with Eq. (15), it can be found that the mechanical stability agrees with the thermodynamics only if the effective mass takes the form [5]

$$\psi \propto \exp(-1/\rho) \quad (16)$$

Any other choices of effective mass will violate the thermodynamic consistency. However, the effective mass in the form of Eq. (16) is often undesirable as it may lead to high spurious velocity and low density contrast. It is worth mentioning that recently Sbragaglia and Shan [24] outlined a systematic procedure on how to construct and derive the effective mass for non-ideal fluids, and provided some criteria on how to adjust the pseudopotential to preserve thermodynamic consistency.

3.2.3. The limited density and viscosity ratios

The original pseudopotential can only achieve a maximum density ratio of the order of $O(10)$. This is acceptable for some cases where the capillary force dominates and the density ratio does not play an important role. A typical example is the two phase capillary flow in the gas diffusion layer of a proton exchange membrane fuel cell (PEMFC) [25]. However, a maximum density ratio of the order of $O(10)$ indeed prevents this model from applying to a wide range of real-world multiphase flow systems (such as bubble flow) where the typical density ratio of $O(1000)$ plays an important role. The viscosity ratio is another concern. In the LB model, a viable way to achieve the large viscosity ratio is to obtain accurate and stable simulations of the single-component multiphase flow in a wide range of viscosity. However, it is found in the pseudopotential model for the single-component multiphase flow, the spurious currents increase as the kinematic viscosity decreases (or the relaxation time approaches 0.5), and the resulting instability often leads to divergences of the simulations [26]. Besides, for most

simulations of multi-component multiphase flow in the literature using the pseudopotential model, the relaxation time for different components is often set as 1, leading to the kinematic viscosity ratio as 1.

3.2.4. The coupling between some properties

The coupling of some properties in the original pseudopotential model is another weakness of this model. In real world, the various aspects of a multiphase system, e.g., the strength of the surface tension, the thickness of the interface, the EOS and its associated properties, are all manifestations of a single microscopic origin, i.e., the interaction potential, and therefore are “coupled together” naturally. However, as a practical numerical tool for simulating engineering problems, it is desirable for those macroscopic properties to be adjustable separately. In the original pseudopotential model with only the first layer of the neighbor nodes employed for the calculation of the interaction force, the density ratio and the surface tension cannot be tuned independently [27]. It is well

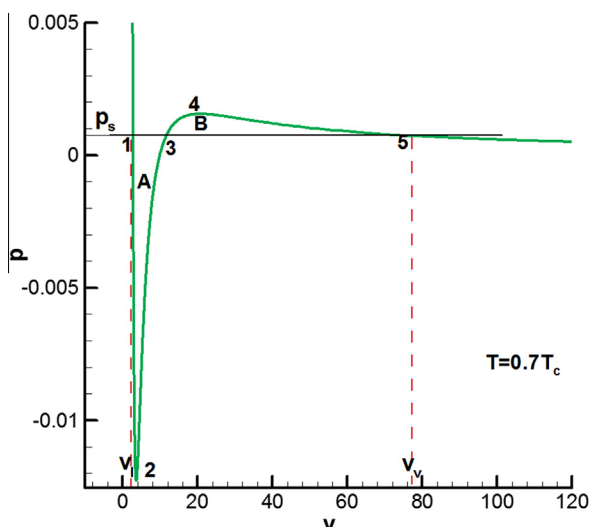


Fig. 4. The p-s curve for C-S EOS at $T = 0.7T_c$. The basic idea of the Maxwell construction is that the area of two regions A (region123) and B (region345) should be equal. p_s is the saturation pressure at the given temperature, and v_l and v_v denote the specific volume of the saturated liquid and saturated vapor.

known that as the size of the system is reduced, the surface tension becomes even more important, and at the meso/micro/nano-scales, may dominate over inertial and gravitational effects. Thus, obtaining desirable surface tension is essential in a multiphase flow model. Another coupling in the original pseudopotential model is the dependence of surface tension and density ratio on the kinematic viscosity. It means that changing the relaxation time leads to the variation of surface tension and density ratio, which is obviously unphysical. Reducing the relaxation time also increases the spurious currents, and when the relaxation time is close to 0.5 the spurious currents are extremely high leading to simulation divergence. It has been demonstrated that the velocity shift force scheme used in the original pseudopotential model is to blame for these dependence [26,28].

4. Improvements of the pseudopotential model

Recently, several techniques/schemes/methods have been developed to alleviate the above limitations of the original pseudopotential model and to improve its performance. These techniques include incorporating realistic EOS into the model [22,29], increasing the isotropy order of the interaction force [27,30], modifying the interaction force [28,31], and improving the force scheme to incorporate the interaction force into the pseudopotential model [28,32–34].

Incorporating proper realistic EOS into the pseudopotential model brings several benefits including reducing the spurious currents and increasing the density ratio [22,29] while minimizing the thermodynamic inconsistency. Recently there has been some work on improving the density ratio for both the single component multiphase flow [22,28] and multi-component multiphase flow [26,35–40]. Incorporating realistic EOS is a critically important scheme for increasing the density ratio [22,28,40]. This approach will be introduced in Section 4.1.

In the original pseudopotential model, only the nearest (1, 2, 3 and 4 in Fig. 1) and next-nearest (5, 6, 7 and 8 in Fig. 1) nodes are used to calculate the interaction force given by Eq. (9), which is referred to E4 isotropy order of the interaction force [27]. With the increase of the isotropy order of the discrete force operator, the spurious current can be greatly reduced [27,30]. In addition, Kupersholt et al. [28] reported that by properly calculating the interaction force via combining the local approximation and the mean-value approximation, the thermodynamic inconsistency of the vdW EOS can be reduced, indicating the proper calculation of the interaction force plays an important role. This conclusion is also demonstrated in Refs. [31,41]. Using high isotropy order of force scheme also can disengage the coupling between the density ratio and the surface tension, making it possible to tune the surface tension independently [27]. This scheme of calculating the interaction force is introduced in Section 4.2.

Grid refinement is helpful for suppressing the spurious currents [27]. The thickness of the phase interface has an important effect on the magnitude of the spurious currents. Increasing the thickness of the interface can reduce the spurious currents. In the framework of multi-range pseudopotential, it is possible to change the interface width while keeping the surface tension and density ratio constant via rescaling the grid system based on certain principles [27]. It is shown that doubling the grid resolution can reduce the amplitude of the spurious currents by nearly an order of magnitude [27]. This technique will be introduced in Section 4.2.2.

Besides, adopting a proper force scheme to incorporate the interaction force into the pseudopotential model helps to diminish the spurious currents, enhance the thermodynamic consistency as well as unravel the coupling between viscosity and surface tension [28,32–34]. Recent studies have found that using a proper

force scheme also facilitates achieving low viscosity [33]. In Section 4.3, different force schemes will be introduced and their performance will be compared based on simulation results in the literature [28,32–34].

Finally, the spurious currents can also be suppressed by using the Multi-relaxation-time (MRT) scheme [26]. Carefully tuning the free parameters in the MRT LB model can effectively decrease the spurious velocity. MRT is also effective to decrease the kinematic viscosity and increase the viscosity ratio [26]. The present review focuses on the SRT LB model, and readers can refer to Refs. [26,42] for details about MRT scheme.

In the following, the techniques/schemes/methods developed to alleviate the limitations of the original pseudopotential model and improve its performance are presented and discussed in detail.

4.1. Incorporation of various equations of state

The typical EOSs are the van der Waals (vdW) EOS, R-K (Redlich-Kwong) EOS, C-S (Carnahan-Starling) EOS and the P-R (Peng-Robinson) EOS. For the details of these EOSs one can refer to [22]. There have been several studies on developing strategies to incorporating different EOS into the pseudopotential model to improve its performance. These strategies are introduced and discussed below.

4.1.1. Yuan and Schaefer's method

In 2006, Yuan and Schaefer [22] developed a relatively simple but effective method to incorporate various EOS into the pseudopotential model. The general idea is to associate the effective mass with different EOS via the following equation, which can be derived from Eq. (12)

$$\psi = \sqrt{\frac{2}{gc_s^2}} (p - \rho c_s^2) \quad (17)$$

The method was also independently proposed by Qin [43] in 2006. With this method, different EOS can be substituted into Eq. (17). For example, for the vdW EOS

$$p = \frac{\rho RT}{1 - b\rho} - a\rho^2 \quad (18)$$

the effective mass can be expressed as

$$\psi = \sqrt{\frac{2}{gc_s^2}} \left(\frac{\rho RT}{1 - b\rho} - a\rho^2 - \rho c_s^2 \right) \quad (19)$$

where a and b are the vdW parameters. The term $1 - b\rho$ accounts for the effects of the non-negligible volume of molecules and $-a\rho^2$ stands for the intermolecular attractions. When Eq. (19) is used in the calculation of the interaction force, the LB fluid then obeys the vdW EOS. Different EOS can be incorporated into the LB model using the same approach, such as the C-S EOS and the P-R EOS. The C-S EOS modifies the first term of the vdW EOS

$$p = \rho RT \frac{1 + bp/4 + (bp/4)^2 - (bp/4)^3}{(1 - bp/4)^3} - a\rho^2 \quad (20)$$

where $a = 0.4963(RT_c)^2/p_c$, $b = 0.1873RT_c/p_c$. Here T_c and p_c are the critical temperature and pressure, respectively. In the present review, without explicitly stated, $a = 1$, $b = 4$ and $R = 1$. The P-R EOS modifies the second term of the vdW EOS

$$p = \frac{\rho RT}{1 - b\rho} - \frac{a\alpha(T)\rho^2}{1 + 2b\rho - b^2\rho^2} \quad (21)$$

$$\alpha(T) = \left[1 + (0.37464 + 1.54226\omega - 0.26992\omega^2) \times (1 - \sqrt{T/T_c}) \right]^2 \quad (22)$$

with $a = 0.45724(RT_c)^2/p_c$, $b = 0.0778RT_c/p_c$.

It is worth mentioning that in the original effective mass given by Eq. (10) used in Refs. [4,5], there is not an explicitly defined temperature. Thus, g in Eq. (12) can be considered to play the role of the temperature. It is known that at the critical point, the first-order and second-order derivatives of the pressure with respect to the density should be zero, namely $dp/d\rho = 0$ and $d^2p/d\rho^2 = 0$. Therefore, one can obtain the critical density ρ_c and the corresponding critical g_c as

$$\rho_c = \rho_0 \ln 2, \quad g_c = -2/(9\rho_0) \quad (23)$$

Here, a temperature-like parameter can be defined as

$$T = -1/g \quad (24)$$

Hence the critical temperature $T_c = 4.5\rho_0$. Then, for $g < g_c$ or ($T < T_c$), two densities of the same material can be observed at a certain pressure, with the lower one as the vapor density and the higher one as the liquid density. Compared with the original effective mass given by Eq. (10), the effective mass corresponding to the vdW/C-S/P-R EOS now has a temperature term. Thus, g becomes unimportant and is only required to guarantee the whole term inside the square root of Eq. (17) to be positive [22]. For example, when Eq. (19) is substituted into Eq. (12), g is canceled out and would not appear in Eq. (18).

With this method of tailoring the expression of the effective mass according to Eq. (17), Yuan and Schaefer [22] thoroughly assessed several EOSs in terms of four criteria. The first criterion is that the achievable maximum density ratio between liquid and vapor should be as large as possible. The second criterion is that the spurious currents at the liquid-vapor interface should be as low as possible. The third criterion is the widest stable temperature range, or the lowest reduced temperature (The reduced temperature is defined as T_{\min}/T_c , where T_{\min} is the minimum temperature). As the temperature becomes continuously lower than T_c , the density ratio goes up and the spurious currents increases. Thus, the achievable stable temperature range is also limited by the spurious currents. The last criterion is the best agreement between the mechanical stability solution and the thermodynamic theory. This criterion is usually evaluated by comparing the coexistence curves obtained from the simulated liquid and vapor densities with the theoretical one predicted by the Maxwell equal-area construction. Yuan and Schaefer [22] found that with a proper EOS the density ratio can be increased to the order of O(1000) with relatively low spurious currents. This is encouraging as it extends the application of the pseudopotential model to most of the real multiphase flow systems with density ratio in the order of O(1000), such as liquid water-vapor system. In addition, Kupershokh recently improved the maximum ratio to be 10^9 with reduced spurious currents by incorporating proper EOS [28]. Yuan and Schaefer [22] found that using proper EOS the thermodynamic inconsistency can also be minimized. They found that the C-S EOS and the P-R EOS give the best thermodynamic consistency while the vdW EOS leads to remarkable thermodynamic inconsistency.

4.1.2. Zhang and Tian's method

Despite the great success of Yuan and Schaefer's method, Zhang and Tian [29] pointed out that this method lost the physical basis of the original Shan and Chen pseudopotential model. In the Yuan and Schaefer method, the effective mass would have the same value for different densities, as can be seen from Fig. 2. For the C-S EOS and the P-R EOS, the effective mass first increases to a peak value and then decreases quickly to zero. Such variation trend leads to the following problems. First, different fluid densities can lead to the same pseudopotential (effective mass). Second, the term inside the square root of Eq. (17) can have zero or even negative values in the region where the effective mass quickly drops, as shown in Fig. 2. Thus the value of g must be switched

between -1 and 1 to keep the term inside the square root of Eq. (17) positive, otherwise the simulation will diverge. It has been pointed out that under such circumstances the calculation of the interaction force will be a problem [41]. In addition, while in the original Shan and Chen pseudopotential model g represents the interaction strength between particles on different locations, in the Yuan and Schaefer's method it is just a local value on a single node and hence no longer has that physical meaning.

In Zhang and Tian's method, they adopted the equilibrium distribution function containing a free parameter d_0 that relates to the sound speed of a component [44]. With such an equilibrium distribution function, the EOS is derived as (for more details, one can refer to [29])

$$p = \frac{1-d_0}{2}\rho + 6g\psi^2 \quad (25)$$

Therefore, different EOS can be incorporated in this method by mapping Eq. (25) to the EOS via reformulating d_0 and g . For example, for the vdW EOS, one can set

$$d_0 = 1 - \frac{2RT}{1-b\rho}, \quad g = -\frac{a}{6}, \quad \psi = \rho \quad (26)$$

Other EOS can be modeled in the similar way.

While Zhang and Tian's method seems to have a more clear physical foundation, it achieves a lower density ratio and leads to relatively large spurious currents compared to the original Shan and Chen model [29], which limits its applications. Therefore, this method needs to be further improved. Currently, the Yuan and Schaefer's method [22] is the most widely used method for incorporating various EOS.

4.2. Calculation of the interaction force

4.2.1. Interaction force with high order isotropy

For most of the applications of Shan and Chen pseudopotential model, only the nearest and next-nearest nodes are considered in the interaction force. For the nearest nodes, namely nodes in the lattice directions 1, 2, 3, 4 as shown in Fig. 1, the weight $w(|\mathbf{e}_z|^2)$ in Eq. (9) is $w(1) = 1/3$, and for the next-nearest one, namely nodes in the lattice direction 5, 6, 7 and 8, the weight $w(|\mathbf{e}_z|^2)$ is $w(2) = 1/12$ [30]. Therefore, for the current computational node (i, j) , Eq. (9) can be written as

$$F_x = -g\psi(i,j)c_s^2 \left[\frac{1}{3}(\psi(i+1,j) - \psi(i-1,j)) + \frac{1}{12}(\psi(i+1,j+1) - \psi(i-1,j+1)) + \frac{1}{12}(\psi(i+1,j-1) - \psi(i-1,j-1)) \right] \quad (27-a)$$

$$F_y = -g\psi(i,j)c_s^2 \left[\frac{1}{3}(\psi(i,j+1) - \psi(i,j-1)) + \frac{1}{12}(\psi(i+1,j+1) - \psi(i-1,j+1)) + \frac{1}{12}(\psi(i+1,j-1) - \psi(i-1,j-1)) \right] \quad (27-b)$$

where F_x and F_y are the force in the x and y direction, respectively. Calculating the interaction force this way yields an isotropy order of 4 and hence is called E4 force scheme. Note that Kang et al. [44] obtained the weights by projection from 4D FCHC (four dimensional face-centered hypercubic lattices [45]), which are consistent with Eq. (27).

Since the RHS of Eq. (9) is the finite difference representation of $-\psi\nabla\psi$, which is obvious in Eq. (11), the interaction force can include any number of neighbor nodes with the properly chosen weights $w(|\mathbf{e}_z|^2)$ for obtaining the highest degree of isotropy [30]. Applying the Taylor expansion to $\psi(\mathbf{x} + \mathbf{e}_z)$, Eq. (9) is rewritten as [27,30]

Table 1

Weights for 4th, 6th and 8th order isotropic tensors in two dimensions [27,30].

Tensor	w(1)	w(2)	w(3)	w(4)	w(5)	w(6)	w(7)	w(8)
E4	1/3	1/12	–	–	–	–	–	–
E6	4/15	1/10	–	1/120	–	–	–	–
E8	4/21	4/45	–	1/60	2/315	–	–	1/5040

$$\mathbf{F} = -g\psi(\mathbf{x})c_s^2 \sum_{n=0}^{\infty} \frac{1}{n!} \nabla^{(n)}\psi(\mathbf{x}) : E^{(n+1)} \quad (28)$$

where $\nabla^{(n)}\psi(\mathbf{x})$ is the rank- n tensor, which means applying the gradient operator ∇ to ψ n times. The symbol “:” denotes full tensor contraction. $E^{(n)}$ is defined as [27,30]

$$E_{i_1 i_2 \dots i_n}^{(n)} = \sum_{\alpha=1}^N w(|\mathbf{e}_\alpha|^2) (\mathbf{e}_\alpha)_{i_1} \dots (\mathbf{e}_\alpha)_{i_n} \quad (29)$$

where N is the number of the neighboring nodes involved. The odd tensor is zero and the even tensor is related to the recursion relation $\Delta^{(n)}$ [27]. The leading terms of Eq. (28) can be expressed in Eq. (11).

With only the first layer of neighboring nodes included, the highest isotropy order is 4 as discussed above. If the neighboring nodes on the second layer are taken into account, tensors of 6th and 8th orders can be made isotropic, and the corresponding weights are listed in Table 1. For higher orders for the 2D and 3D cases, one can refer to [27,30]. Here we present the expressions of the interaction force values with E8 tensor

$$\begin{aligned} F_x = -g\psi(i,j)c_s^2 & \left[\frac{4}{21}(\psi(i+1,j) - \psi(i-1,j)) + \frac{4}{45}(\psi(i+1,j+1) \right. \\ & - \psi(i-1,j+1)) + \frac{4}{45}(\psi(i+1,j-1) - \psi(i-1,j-1)) \\ & + \frac{1}{60}(2\psi(i+2,j) - 2\psi(i-2,j)) + \frac{2}{315}(2\psi(i+2,j+1) \\ & - 2\psi(i-2,j+1)) + \frac{2}{315}(2\psi(i+2,j-1) - 2\psi(i-2,j-1)) \\ & + \frac{2}{315}(\psi(i+1,j+2) - \psi(i-1,j+2)) + \frac{2}{315}(\psi(i+1,j-2) \\ & - \psi(i-1,j-2)) + \frac{1}{5040}(2\psi(i+2,j+2) - 2\psi(i-2,j+2)) \\ & \left. + \frac{1}{5040}(2\psi(i+2,j-2) - 2\psi(i-2,j-2)) \right] \end{aligned} \quad (30-a)$$

$$F_y = -g\psi(i,j)c_s^2 \left[\begin{aligned} & \frac{4}{21}(\psi(i,j+1) - \psi(i,j-1)) + \frac{4}{45}(\psi(i+1,j+1) - \psi(i+1,j-1)) \\ & + \frac{4}{45}(\psi(i-1,j+1) - \psi(i-1,j-1)) + \frac{1}{60}(2\psi(i,j+2) - 2\psi(i,j-2)) \\ & + \frac{2}{315}(\psi(i+2,j+1) - \psi(i+2,j-1)) + \frac{2}{315}(\psi(i-2,j+1) - \psi(i-2,j-1)) \\ & + \frac{2}{315}(2\psi(i+1,j+2) - 2\psi(i+1,j-2)) + \frac{2}{315}(2\psi(i-1,j+2) - 2\psi(i-1,j-2)) \\ & + \frac{1}{5040}(2\psi(i+2,j+2) - 2\psi(i+2,j-2)) + \frac{1}{5040}(2\psi(i-2,j+2) - 2\psi(i-2,j-2)) \end{aligned} \right] \quad (30-b)$$

It has been demonstrated that the relatively large spurious currents in the vicinity of the curved phase interface in the original pseudopotential model result from insufficient isotropy of the interaction force [30]. With the increased isotropy, the spurious currents can be remarkably reduced. Fig. 3 shows the simulated spurious currents around a droplet in a periodic gravity-free domain with a 201×201 lattice system. In the simulation, a liquid droplet with initial radius r_0 is placed at the center of the domain. The density field is initialized using the method in Ref. [32].

$$\rho(i,j) = \frac{\rho_{\text{liquid}} + \rho_{\text{vapor}}}{2} - \frac{\rho_{\text{liquid}} - \rho_{\text{vapor}}}{2} \times \tanh \left[\frac{2 \left(\sqrt{(i - i_{\text{center}})^2 + (j - j_{\text{center}})^2} - r_0 \right)}{W} \right] \quad (31)$$

where ($i_{\text{center}} = 101, j_{\text{center}} = 101$) is the center position of the domain. ‘tanh’ is the hyperbolic tangent function and $\tanh(x) = (e^{2x} - 1)/(e^{2x} + 1)$. W is the prescribed width of the phase interface and is usually varied by 1–5 lattices. Values for ρ_{liquid} and ρ_{vapor} are set as the theoretical densities predicted by Maxwell equal-area construction at the corresponding temperature. C-S EOS is adopted and $T = 0.7T_c$. The force scheme for incorporating the interaction force into the LB model is the velocity shift force scheme (see Section 4.3). It is worth mentioning that using Eq. (31) to initialize the system leads to a smooth transition of the density field and helps improve the numerical stability in the initial several iteration steps. As can be seen from Fig. 3, the maximum spurious current with E8 tensor is only 0.007, half of that by using E4 tensor, indicating using higher order isotropy can reduce the spurious currents.

As pointed out previously, the RHS of Eq. (9) is the finite difference representation of $-\psi\nabla\psi$. Noting that $\psi\nabla\psi = 0.5\nabla\psi^2$, the interaction force also can be alternatively calculated by

$$\mathbf{F}(\mathbf{x}) = -\frac{g}{2} c_s^2 \sum_{\alpha=1}^N w(|\mathbf{e}_\alpha|^2) \psi^2(\mathbf{x} + \mathbf{e}_\alpha) \mathbf{e}_\alpha \quad (32)$$

Note that Eq. (9) contains the effective mass of the current lattice as well as that of the neighboring lattices, while Eq. (32) involves only the effective mass of the neighboring nodes. It is found that combining Eqs. (9) and (32) can extend the stable temperature range, diminish the spurious currents and reduce the thermodynamic inconsistency [28,31]

$$\begin{aligned} \mathbf{F}(\mathbf{x}) = -\beta \frac{g}{2} c_s^2 \sum_{\alpha=1}^N w(|\mathbf{e}_\alpha|^2) \psi^2(\mathbf{x} + \mathbf{e}_\alpha) \mathbf{e}_\alpha \\ - \frac{1-\beta}{2} g\psi(\mathbf{x}) c_s^2 \sum_{\alpha=1}^N w(|\mathbf{e}_\alpha|^2) \psi(\mathbf{x} + \mathbf{e}_\alpha) \mathbf{e}_\alpha \end{aligned} \quad (33)$$

where β can be tuned to greatly reduce the thermodynamic inconsistency. For more details of such treatment, one can refer to [28,31].

4.2.2. Midrange attractive interactions

One drawback of the interaction force scheme in Section 4.2.1 is that there is only a single free parameter g . Thus, both the surface tension and the density ratio change as g changes. As mentioned previously, when a realistic EOS is incorporated using Yuan and Schaefer's method [22], g no longer plays the role of the strength of the interaction force. Rather, its sole function is to keep the term in the square root of Eq. (17) positive. Under such circumstances, both the surface tension and the density ratio change as temperature changes. Therefore, the surface tension and the density ratio

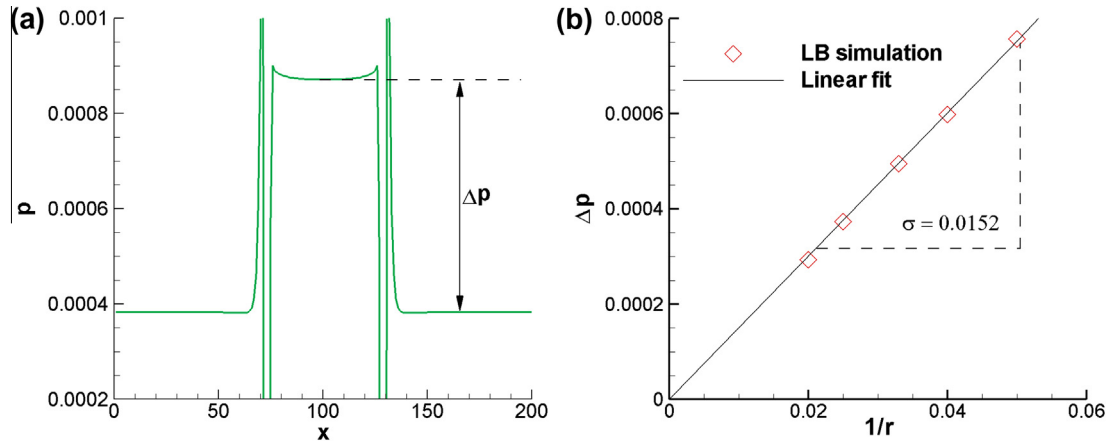


Fig. 5. Simulation results of a circular static liquid droplet embedded in a vapor phase in a gravity-free field using a 201×201 lattices periodic system. (a) Pressure distribution along the horizontal center of the computational domain. The initial droplet radius is 30 lattices and $T = 0.7T_c$. (b) Summary of LB results for droplet with different radius and calibration of the Laplace law at $T = 0.7T_c$. (Reproduced from Chen et al. [46].)

are not independently tunable when Eq. (9) is employed to calculate the interaction force. This is the coupling between surface tension and density ratio as discussed in Section 3.2.4. Such interdependence is analyzed more theoretically as follows. The analytical value of the surface tension can be derived based on a two-phase system with a flat interface having a constant pressure in both phases far from the interface [5]. The surface tension is the integral across the flat interface of the difference between the normal pressure (y direction) tensor and the transversal pressure tensor (x direction), and its analytical value is given by [5]

$$\sigma = -\frac{gc_s^4}{2} \int_{-\infty}^{+\infty} (\partial_y \psi)^2 dy \quad (34)$$

It can be seen from Eqs. (12) and (34) that the surface tension and the EOS is controlled by the single free parameter g .

Before reviewing about the scheme to tune the surface tension and EOS separately, we want to discuss the simulation of surface tension. The typical numerical experiment to assess the surface tension is to simulate a droplet (bubble) surrounded by gas (liquid) in a periodic gravity-free domain. Laplace law is used to calculate the surface tension force, which states that the pressure jump across the phase interface is linearly proportional to the reciprocal of the radius of the droplet (bubble), and the slope of the line is the surface tension force. The Laplace law is expressed as

$$\nabla p = p_{\text{in}} - p_{\text{out}} = \frac{\sigma}{r} \quad (35)$$

where p_{in} and p_{out} are the fluid pressures inside and outside of the droplet (bubble), respectively. r is the radius of the droplet (bubble) and σ is the surface tension. In the simulations, a circular static liquid droplet is embedded in the vapor phase in a gravity-free field. The initial and boundary condition is the same to that in Fig. 3. A series of simulations are conducted by changing r_0 . Δp is calculated as the difference between the steady-state high pressure inside the droplet and the steady-state low pressure outside the droplet, as shown in Fig. 5(a). Note that large fluctuations of the pressure near the liquid-vapor interface are unphysical due to sharp change of density and are ignored when calculating Δp . Fig. 5(b) plots Δp as a function of $1/r$, where the linear relationship can be clearly observed. The slope of the line is the surface tension σ which is assessed as 0.0152 [46].

In 2007, Sbragaglia et al. [27] introduced a second attractive force term into the interaction force given by Eq. (9)

$$\mathbf{F}(\mathbf{x}) = -g_1 \psi(\mathbf{x}) c_s^2 \sum_{\alpha=1}^N w(|\mathbf{e}_\alpha|^2) \psi(\mathbf{x} + \mathbf{e}_\alpha) \mathbf{e}_\alpha - g_2 \psi(\mathbf{x}) c_s^2 \sum_{\alpha=1}^N w(|\mathbf{e}_\alpha|^2) \psi(\mathbf{x} + 2\mathbf{e}_\alpha) \mathbf{e}_\alpha \quad (36)$$

With the second term on the RHS, the EOS is similar to that given by Eq. (12) with g in Eq. (12) replaced by $A_1 = g_1 + 2g_2$. However, the surface tension now becomes [27]

$$\sigma = -\frac{A_2 c_s^4}{2} \int_{-\infty}^{+\infty} (\partial_y \psi)^2 dy \quad (37)$$

with $A_2 = g_1 + 8g_2$. It is obvious that now there are two tunable parameters g_1 and g_2 . Therefore, the density ratio and the surface tension can be changed independently. By keeping A_1 constant, namely fixing the EOS, the surface tension can be tuned independently by changing only A_2 . Simulations were performed in Ref. [27] by changing A_2 and fixing A_1 , and it is found that the width of the phase interface changes with A_2 while the density ratio is the same (Fig. 1 in Ref. [27]). Spreading the density difference across the phase interface over a larger number of lattices obviously can increase the numerical stability.

With an effective mass in the form of $\psi = \sqrt{\rho_0}(1 - \exp(-\rho/\rho_0))$, Sbragaglia et al. [27] noted that besides A_1 and A_2 , there is another free parameter, namely ρ_0 , by tuning which the interface resolution can be enhanced. By varying A_2 according to $A'_2 = A_2 \rho_0^2$ and re-scaling the grid system with $\Delta x' = \rho_0 \Delta x$, the interface width can be changed when ρ_0 is tuned, while the density ratio and the surface tension can be kept constant. It was found that by changing ρ_0 from 1 to 0.5, the maximum spurious current was decreased almost ten times, although more computational resources are required when refined grid system is adopted.

4.2.3. Middle-range repulsion force

In the pseudopotential model, only the attractive force is imposed between the fluid particles, and it induces the phase separation by a dynamic instability of the phase interface [47]. However, the instability is not possible in physical reality as it is tamed by the hard-core repulsion that is ignored in the Shan and Chen pseudopotential model [47]. Therefore, Chibbaro et al. [47] further introduced midrange repulsion force into Eq. (9). It is known that generally only one droplet can be formed when performing the simulation of first order phase segregation (Fig. 6(a)) using the original pseudopotential model. This is because

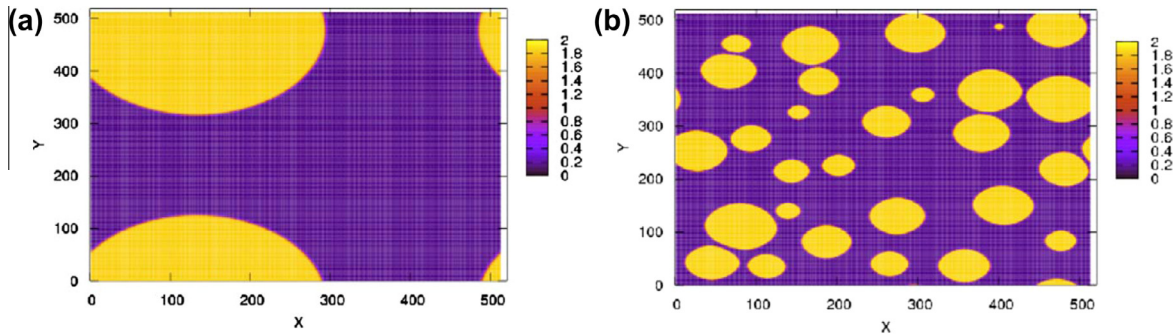


Fig. 6. Spatial distribution of the fluid density (a) the pseudopotential model without midrange repulsion force and (b) with midrange repulsion force. The formation of multi-droplet in Fig. b due to the midrange repulsion force can be clearly observed. (Reproduced from Chibbaro et al. [47].)

without the repulsive force, the disjoining pressure is negative and thus the thin films between the disperse phase (droplets or bubbles) will rupture, leading to a single droplet. With a repulsive force, the disjoining pressure turns to be positive, with which the thin film becomes stable and the overlap of phase interfaces is prevented [48]. Thus, the formations of spray-like, multi-droplet configurations are captured and the surface-volume ratio is greatly increased (Fig. 6(b)). Such midrange repulsion force offers the possibility to capture an entirely new set of physical regimes and has potential applications in complex multiphase flows including atomization, spray formation, micro-emulsions and soft-glassy system [48–51].

4.3. Force schemes

In general, the total force acting on a fluid particle in multiphase flow includes

$$\mathbf{F} = \mathbf{F}_f + \mathbf{F}_{ads} + \mathbf{F}_b \quad (38)$$

where \mathbf{F}_{ads} is the solid–fluid interaction force and will be introduced in Section 5, \mathbf{F}_f is the fluid–fluid interaction force and \mathbf{F}_b represents other possible external forces such as gravitational and electrical forces.

Multiphase flow in which the gravitational force plays an important role is widely encountered, such as bubble rising under the influence of gravitational force. There are several ways of introducing the gravitational force. Gravity force can be applied uniformly in the entire domain

$$\mathbf{F}_g = \rho g \quad (39)$$

Another method of introducing gravitational force is as follows

$$\mathbf{F}_g = \rho \mathbf{g} \left(1 - \frac{\langle \rho \rangle}{\rho} \right) \quad (40)$$

where $\langle \rho \rangle$ is the average density in the entire domain and ρ is the density at the current node. Using Eq. (40) can ensure a zero external force averaged in the entire domain, thus keeping the mass-average velocity of the system constant. In addition, the gravity force can also be calculated using the following expression

$$\mathbf{F}_g = \mathbf{g}(\rho - \rho_g) \quad (41)$$

which means that the force only affects the liquid phase. Whether the above methods of introducing the gravitational force predict the same multiphase behavior or not depends on the particular problems simulated [52]. Our preliminary simulations on a bubble rising in a two-dimensional bounded domain (with solid walls in all the directions) under gravitational force indicate that the way of calculating the gravitational force indeed affects the numerical stability, and Eq. (40) performs best especially for multiphase flow

with high density ratios. Note that for a periodic domain, Eq. (40) should be adopted, otherwise the rising bubbles will drag the liquid along with them and the two phase mixture will continue to accelerate upwards, as there is no solid wall which can provide the drag force to balance the gravitational force [53].

How to implement the total force given by Eq. (38) into the LB framework is very important for the numerical stability and accuracy of the pseudopotential model. There are three force schemes widely used, including the velocity shift force scheme (the original Shan and Chen force scheme [4]), the exact difference method (EDM) scheme [28] and Guo's force scheme [54]. These force schemes are briefly introduced as follows.

4.3.1. Velocity shift force scheme

The velocity shift force scheme is the original force scheme that Shan and Chen used [4]. In this scheme, the interaction force is incorporated into the model by shifting the velocity \mathbf{u} in the equilibrium distribution function, with which \mathbf{u} is replaced by \mathbf{u}^{eq}

$$\mathbf{u}^{eq} = \mathbf{u} + \frac{\tau}{\rho} \mathbf{F} \Delta t \quad (42)$$

where \mathbf{u} is given by Eq. (5). By averaging the momentum before and after the collision step, the actual physical velocity is given by

$$\mathbf{u}_p = \mathbf{u} + \frac{1}{2\rho} \mathbf{F} \Delta t \quad (43)$$

Note that the fore term in the RHS of Eq. (1) is not needed when the velocity shift force scheme is adopted. This velocity shift force scheme is a unique feature of the original pseudopotential model.

4.3.2. Exact difference method (EDM)

The EDM force scheme was proposed by Kupershtokh et al. [28]. This method was directly derived from the Boltzmann equation. In this force scheme, the force term in Eq. (1) is given by

$$F_x = f_x^{eq}(\rho, \mathbf{u} + \mathbf{F} \Delta t / \rho) - f_x^{eq}(\rho, \mathbf{u}) \quad (44)$$

where \mathbf{u} is given by Eq. (5). F_x is simply the difference of equilibrium distribution functions corresponding to the mass velocity after and before the action of particle interaction force \mathbf{F} . The real fluid velocity in the EDM is also calculated by Eq. (43).

4.3.3. Guo's force scheme

In 2002, Guo et al. [54] proposed a force scheme by directly adding the discrete form of the force to the evolution equation of the distribution function with the consideration of the discrete lattice effect and the contribution of the force to the momentum flux. In this force scheme, the last term in Eq. (1) is given by

$$F_x = \left(1 - \frac{1}{2\tau} \right) \omega_x \left(\frac{\mathbf{e}_x - \mathbf{u}^{eq}}{c_s^2} + \frac{\mathbf{e}_x \mathbf{u}^{eq}}{c_s^4} \right) \cdot \mathbf{F} \Delta t \quad (45)$$

In this force scheme, the real fluid velocity and the equilibrium velocity are expressed in the same form

$$\mathbf{u}_p = \mathbf{u}^{eq} = \mathbf{u} + \frac{1}{2\rho} \mathbf{F} \Delta t \quad (46)$$

Besides the above force schemes which are widely adopted in the pseudopotential multiphase LB model, there are other force schemes such as Ladd and Verberg's force scheme [55], Luo's force scheme [56] and He's force scheme [9]. Recently, Huang et al. [32], Li et al. [33] and Sun et al. [34] thoroughly evaluated the performance of different force schemes in terms of the spurious currents, stable temperature range, maximum density ratio, and agreement of the coexistence curves. It is found that: (1) for the dependence of the surface tension and density on the kinematic viscosity, i.e., the relaxation time, both the EDM and Guo's force scheme lead to independence, while in the velocity shift scheme the surface force and density change with the kinetic viscosity; (2) for the stable temperature range, Guo's force scheme leads to a relatively narrow temperature range. For example, at $\tau = 1$ for C-S EOS, the minimum T_{min} achieved is only $T_{min} = 0.777T_c$. The velocity shifting scheme and the EDM scheme are demonstrated to perform almost the same for $\tau = 1$. When $\tau < 1$, the EDM performs better than the velocity shifting scheme, while for $\tau > 1$ the performance is opposite (see Fig. 7 in Ref. [32] and Fig. 1 in Ref. [33]); (3) for the thermodynamic coexistence, Guo's model gives the best agreement, while the discrepancy between the density of the simulation results using the EDM and that predicted by the Maxwell equal-area construction techniques increases as the temperature decreases.

5. Fluid–solid interaction: contact angle

So far, the discussion has not involved the fluid–solid interactions. Wetting phenomena are not only widespread in nature but also play an important role in many scientific and industrial processes. For most problems involving surface effects, fluid–solid interactions are particularly important for meso-/micro-/nano-scale devices, where the physical behavior is largely affected by high surface/volume ratios [57]. Contact angle is usually considered as a measure of the solid surface wettability. It is defined as the angle at which the fluid/fluid interface meets a solid phase. A fluid is wetting if its contact angle $\theta < 90^\circ$, and this fluid tends to spread as a film on the solid surface. On the contrary, the fluid is non-wetting if $\theta > 90^\circ$, and the fluid tends to form a droplet on the solid surface.

The fluid–solid interaction and wetting conditions can be easily implemented in the pseudopotential model. The adhesion force between the fluid and the solid wall can be calculated by the following general form [45], which is similar to Eq. (9)

$$\mathbf{F}_{ads}(\mathbf{x}) = -g_w \psi(\mathbf{x}) \sum_{\alpha=1}^N w(|\mathbf{e}_\alpha|^2) \psi(\rho_w) s(\mathbf{x} + \mathbf{e}_\alpha) \mathbf{e}_\alpha \quad (47)$$

where s is an indicator function that equals 1 for solid nodes and 0 for fluid nodes. g_w and ρ_w can be tuned separately or jointly to achieve different contact angles. There are generally three methods to obtain different contact angles. First, a widely used approach is fixing $\psi(\rho_w) = 1$ and changing g_w to achieve the desired contact angle. Positive and positive value of g_w leads to $<90^\circ$ (hydrophilic) and $>90^\circ$ (hydrophobic) contact angle, while $g_w = 0$ results in the contact angle of 90° . Second, one also can fix g_w and changing ρ_w to obtain the desired contact angle. Here the solid phase is perceived as carrying a fictitious density ρ_w . Note this fictitious density is not the realistic density of the material of the solid phase. For a liquid–vapor system with densities of liquid and vapor as ρ_l and ρ_g , respectively, setting $\rho_w = \rho_l$ leads to $\theta = 0^\circ$ and setting $\rho_w = \rho_g$

results in $\theta = 180^\circ$, and changing ρ_w in the range of (ρ_g, ρ_l) the contact angle can span the range $(0^\circ, 180^\circ)$ [57]. Note that the density of the solid phase is a fixed value and is not evolving with the LB equation. Last but not least, tuning g_w and ρ_w jointly provides more flexibility for obtaining different contact angles, and one can refer to [57] for more details.

The typical simulation experiment for obtaining different contact angles is via putting an initially semicircular static droplet on a flat homogeneous solid surface and changing \mathbf{F}_{ads} . Here an example of using the first method of changing g_w and fixing $\psi(\rho_w) = 1$ is presented. An initially semicircular static droplet with a radius of 30 lattices is placed on a horizontal solid surface and g_w is changed in the range from -0.2 to 0.1 . The simulations are performed in a 201×201 lattice system with the top and bottom boundaries as solid walls and the left and right boundaries as periodic boundaries. C–S EOS is used and the temperature is $T = 0.7T_c$. The insets in the figure show typical droplets with different contact angles. After the simulation is converged, the base length b and the height h of the droplet are measured. To this end, phase interface should be determined which is defined at the position where the density is $(\rho_l + \rho_g)/2$. The contact angle can be calculated by

$$r = \frac{(4h^2 + b^2)}{8h} \quad (48-a)$$

$$\theta = \begin{cases} \arcsin\left(\frac{h}{2r}\right), & \theta \leqslant 90^\circ \\ \pi - \arcsin\left(\frac{h}{2r}\right), & \theta > 90^\circ \end{cases} \quad (48-b)$$

Fig. 7 demonstrates that different contact angles can be obtained by tuning g_w .

Unlike the traditional top down approach where macroscopic properties including surface tension and contact angle can be prescribed, in the pseudopotential model, the value of the contact angle is not known “*a priori*”, although there is a functional relationship between the static contact angle and the interaction strength, such as that in **Fig. 7**. Recently, Huang et al. [58] proposed an empirical scheme for “*a priori*” contact angle determination, making it possible to estimate “*a priori*” the value of the contact angle.

6. Multi-component pseudopotential model

The above review is mainly on the single-component multiphase (SCMP) flow. Now attention is turned to multi-component multiphase (MCMP) flow. MCMP flow systems are widely encountered in nature and engineering, such as liquid water–air flow and liquid water–oil flows. For multi-component pseudopotential model, the interaction force between fluid components σ and $\bar{\sigma}$ is introduced which is similar to that of Eq. (9)

$$\mathbf{F}_{\sigma\bar{\sigma}}(\mathbf{x}) = -g_{\sigma\bar{\sigma}} \psi_\sigma(\mathbf{x}) c_s^2 \sum_{\alpha=1}^N w(|\mathbf{e}_\alpha|^2) \psi_{\bar{\sigma}}(\mathbf{x} + \mathbf{e}_\alpha) \mathbf{e}_\alpha \quad (49)$$

where $g_{\sigma\bar{\sigma}}$, the interaction strength between different components, is set positive to mimic repulsion force. The original effective mass given by Eq. (10) can be adopted by each component in the MCMP pseudopotential model. Another widely adopted effective mass for each component is taking the form of the density itself. The force scheme introduced in Section 4.3 can be employed to incorporate the force into the pseudopotential model. The EOS of the system is calculated by

$$p = \sum \rho_\sigma c_s^2 + \frac{c_s^2}{2} \sum g_{\sigma\bar{\sigma}} \psi_\sigma \psi_{\bar{\sigma}} \quad (50)$$

For a two-component multiphase system, there are three interaction strength namely $g_{\sigma\sigma}$, $g_{\sigma\bar{\sigma}}$ ($g_{\sigma\bar{\sigma}} = g_{\bar{\sigma}\sigma}$), and $g_{\bar{\sigma}\bar{\sigma}}$. In most studies

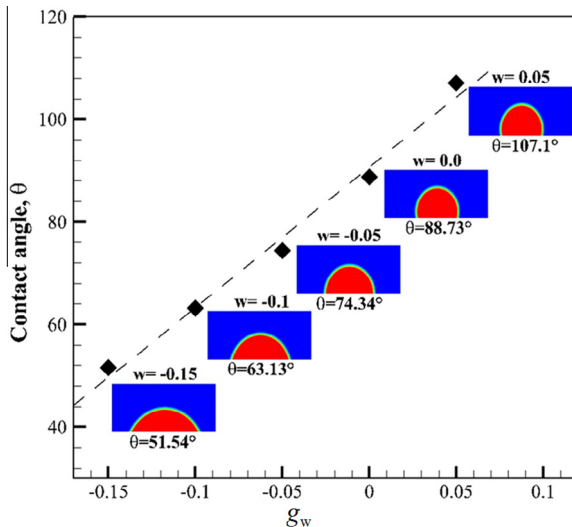


Fig. 7. (Color online) Simulation results of different equilibrium contact angles for a liquid droplet on a flat and uniform solid wall with different liquid-solid strength g_w . The insets show droplets with different contact angles. The system is a gravity-free field with top and bottom solid walls and periodic left and right boundaries. The system is discretized by 201×201 lattices. C-S EOS is used and $T = 0.7T_c$. The initial radius of the droplet is 30 lattices.

employing the MCMP pseudopotential model, the interaction strength within each component, namely $g_{\sigma\sigma}$ and $g_{\bar{\sigma}\bar{\sigma}}$, is set as zero, and only the interaction between different components $g_{\sigma\bar{\sigma}}$ contributes to the phase separation. Increasing $g_{\sigma\bar{\sigma}}$ to a critical value, the fluid mixture separates into two fluids and an interface forms between the two fluids. As $g_{\sigma\bar{\sigma}}$ is further increased, the width of the interface reduces and the solubility of one component in the other declines. However, a too large value of $g_{\sigma\bar{\sigma}}$ can lead to a negative density of one component in the other. Unfortunately, by using only one free parameter $g_{\sigma\bar{\sigma}}$ to control the two-fluid system, the density ratio between the components is only unit and the maximum kinematic viscosity ratio achievable is less than 5 [59,60].

Until very recently, there have been very few studies focusing on increasing the density ratio between different components [26,35–40]. It is worth mentioning that the first step to increase the density ratio between different components is to enhance the density difference between the liquid phase and gas phase of the same component. To this end, the interaction forces between the same component, namely $g_{\sigma\sigma}$ and $g_{\bar{\sigma}\bar{\sigma}}$ now play dominant roles, compared with the interaction strength between different component $g_{\sigma\bar{\sigma}}$. Since a MCMP system with a large density ratio is often a liquid-gas system, we discuss in this scenario for simplicity. The gas component usually can be considered as an ideal gas, hence the interaction force $g_{\bar{\sigma}\bar{\sigma}}$ (here the component $\bar{\sigma}$ denotes gas component and σ stands for the liquid component) is set to zero, leading to the ideal EOS for the gas phase. For the non-ideal liquid component, $g_{\sigma\sigma}$ starts to play a role. If the effective mass in the form of Eq. (10) is used, increasing $|g_{\sigma\sigma}|$ leads to a higher density ratio within the same component, which further helps rise the density ratio between different components [26,36,37]. Nevertheless, the maximum density ratio obtained by using Eq. (10) for the non-ideal component is still limited and far from satisfactory. Very recently, several studies have been reported on incorporating real EOS into the liquid component for achieving high density ratio of O(1000) between the liquid component and gas component [39,40,61]. The simulation of the MCMP system is still stable with density ratio of the order O(100) when relatively fast fluid flow is considered [39]. It is worth mentioning that for such liquid-gas MCMP system, an effective mass for the gas component $\bar{\sigma}$

required when calculating the interaction force between different components, although the gas component is an ideal gas. The typical form is $\psi_{\bar{\sigma}} = \rho$ [37] or $\psi_{\bar{\sigma}} = \sqrt{\rho}$ [38]. The interaction strength $g_{\sigma\bar{\sigma}}$ now is set as a small value compared to $g_{\sigma\sigma}$, which affects the solubility of one component in the other.

Finally, for a MCMP system with all the components as non-ideal components, interaction strength within each component should be no-zero and non-ideal EOS can be incorporated for each component [40]. In summary, the total force acting on a component now includes inter-component interaction force and intra-molecule interaction, which is expressed

$$\mathbf{F}_{\sigma}(\mathbf{x}) = -g_{\sigma\sigma}\psi_{\sigma}(\mathbf{x})c_s^2 \sum_{\alpha=1}^N w(|\mathbf{e}_{\alpha}|^2)\psi_{\sigma}(\mathbf{x} + \mathbf{e}_{\alpha})\mathbf{e}_{\alpha} \\ - g_{\sigma\bar{\sigma}}\psi_{\sigma}(\mathbf{x})c_s^2 \sum_{\alpha=1}^N w(|\mathbf{e}_{\alpha}|^2)\psi_{\sigma}(\mathbf{x} + \mathbf{e}_{\alpha})\mathbf{e}_{\alpha} \quad (51)$$

$$\mathbf{F}_{\sigma}(\mathbf{x}) = -g_{\sigma\sigma}\psi_{\sigma}(\mathbf{x})c_s^2 \sum_{\alpha=1}^N w(|\mathbf{e}_{\alpha}|^2)\psi_{\sigma}(\mathbf{x} + \mathbf{e}_{\alpha})\mathbf{e}_{\alpha} \\ - g_{\bar{\sigma}\bar{\sigma}}\psi_{\sigma}(\mathbf{x})c_s^2 \sum_{\alpha=1}^N w(|\mathbf{e}_{\alpha}|^2)\psi_{\sigma}(\mathbf{x} + \mathbf{e}_{\alpha})\mathbf{e}_{\alpha} \quad (52)$$

It is found, however, when using Eq. (49) to calculate the interaction force between different components, the mutual diffusivity is so small that it is difficult to reach equilibrium even after very long time simulation [62,63]. The distributions of the components in the gas phase show discontinuous patterns. Therefore, to increase the mutual diffusivity, a modified equation is proposed to calculate the intra-molecule interaction [62,63].

Similar to Eq. (47), the fluid–solid interaction force is calculated by

$$\mathbf{F}_{\sigma,\text{ads}}(\mathbf{x}) = -g_{\sigma w}\psi(\mathbf{x}) \sum_{\alpha=1}^N w(|\mathbf{e}_{\alpha}|^2)\psi(\rho_w)s(\mathbf{x} + \mathbf{e}_{\alpha})\mathbf{e}_{\alpha} \quad (53)$$

For two components systems, usually $g_{\sigma w} = -g_{w\sigma}$. Different contact angles can be obtained by the same methods introduced in Section 5.

As previously stated in Section 4.2.2, the surface tension expressed by Eq. (34) is obtained from the pressure tensor. The pressure tensor due to molecular force is a crucial variable based on which many macroscopic properties can be obtained such as density profile and surface tension [18,64]. Calculating the pressure tensor properly is thus of significant importance. Shan et al. [18] derived the correct form of the pressure tensor through its basic definition – the momentum transfer rate through an area of surface. Following Ref. [18], Sbragaglia and Belardinelli further extended the derivation to multi-component system [64].

7. Applications

In this section, we review some representative applications of the pseudopotential model. Due to its computational efficiency and conceptual simplicity, the pseudopotential model has been an effective and powerful technique for simulating multiphase flow problems, particularly for flows with complex topological changes of the interface (deformation, coalescence, breakup, etc.) or in complex geometries, and has drawn extensive attention of researchers in a broad range of sciences including energy, environment, chemistry, biology and geology. It has been widely used for simulating multiphase flows such as droplet behaviors (droplet coalescence/split/collision, droplet sliding on smooth or rough solid surface, droplet formation, etc.), bubble behaviors, contact line movement and multiphase flow in porous media. It also has

been coupled with other models for more complex thermal reactive transport processes such as coupling with heat transfer model for phase change heat transfer problem, coupling with suspension particle model for multiphase suspension system, and coupling with mass transport model for reactive transport processes. Recently, it has also been considered as a super-molecular method and has provided an alternative way to explore slippage phenomena on solid boundary.

7.1. Droplet/bubbles behaviors and contact line movement

The pseudopotential model has been successfully applied to simulate contact line movement and droplet/bubble behaviors with and without solid walls, including droplet dynamic behaviors on a solid surface under gravitational force [44,60,65], droplet motion, coalescence and split behaviors on solid surface with patterned wettability gradients [31,66–68], impingement of liquid droplets onto a dry surface [69–71], highly controlled formation of droplets in micro-channel [72–75], droplet wetting phenomena on super-hydrophobic surface [76–78], cavitation phenomena [79], capillary rise between parallel plates [80–82], capillary filling [83–85], droplets in turbulent flow [86], droplet under the effects of an external magnetic field [87,88], bubble rising in stagnant liquid under gravitational force [26,35–37,53,89], and spinodal phase separation [90–92].

7.1.1. Droplet sliding on a solid surface

Droplet dynamic behaviors on a solid surface under gravitational force have been successfully studied using the pseudopotential model. Kang et al. adopted the MCMP to study the displacement of an immiscible droplet subject to the gravitational force in a 2D channel [44] as well as in a 3D duct [60]. The former study is the first work in which the weights for nearest and next-nearest interactions in D2Q9 lattice model were derived by projecting the FCHC (face-centered hyper-cube) lattice onto the D2Q9 lattice. Dynamic behavior of a droplet was analyzed, and the effects of contact angle, Bond number Bo (the ratio of the body force to the surface tension force), droplet size, and density and viscosity ratios of the droplet to the displacing fluid were investigated. Their findings include a critical Bo for a given static contact angle, above which no steadily sliding droplet is observed. The value of the critical Bo decreases as the contact angle increases. For a Bo above the critical value, increasing the contact angle results in a larger fraction of the droplet entrained in the bulk.

Fig. 8 presents the simulation results of dynamic behaviors of a 3D droplet in the duct with $Ca = 0.66$ (the ratio of viscous force to surface tension force) and contact angle of 90° [60]. It can be seen that under the gravitational force, the droplet is elongated and the wetting length increases continuously. A neck forms between the base of the droplet and its front. After the neck breaks, a portion of the droplet pinches off and is entrained into the bulk flow. The remaining part of the droplet contacting with the solid walls shrinks due to the surface tension force.

The solid surface structures play an important role in the dynamic behaviors of the droplet. Very recently, Mazloomi and Moosavi [65] further adopted the MCMP pseudopotential model to study a similar 2D problem with U-shape and V-shape grooves on the solid surface. Emphasis was placed on studying the covering of the grooves by the liquid phase under different width, depth and gaps of the grooves. It was found that for a groove there is a critical width above which the groove can be coated successfully. The critical width depends on the capillary number, the contact angle, the geometry, and the depth of the groove. The covering of the second groove not only depends on the geometries of itself but also is affected by the first groove.

Understanding the droplet motion, coalescence and split behaviors on solid phase with patterned wettability gradients is of great importance to micro-nano-fluidic devices. Gong and Cheng [31] employed the SCMP pseudopotential model to study 3D droplet motion and coalescence processes driving by wettability gradients on solid surfaces. Different forms of the wettability gradient on the solid surface were considered and the driving mechanisms of the droplet motion were investigated in detail. Clime et al. [66,67] also studied the droplet motion and coalescence on a mixed wetted solid surface using the SCMP pseudopotential model. The background of their study was the transport of droplets in digital micro-fluidic devices where the contact angle gradient was generated by applying electrical potential difference between the solid and the liquid (electrowetting effect). The coalescence and splitting of droplets under different contact angles and different geometries were investigated. Dörfler et al. [68] adopted the MCMP pseudopotential model to explore the motion of thin liquid film lying on top of chemical patterns on a substrate. Their studies focus on open microfluidic system in which droplets and rivulets were confined to hydrophilic channels on a hydrophobic or less hydrophilic substrate. The two phases simulated were immiscible oil–water system. It was found that the patterned hydrophilic channel can successfully guide the motion of the liquid water, although

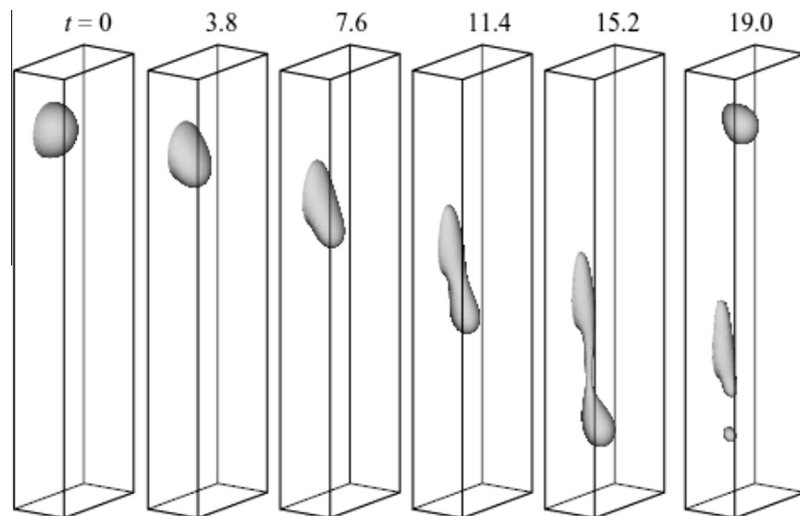


Fig. 8. Dynamic behavior of the droplet at $Ca = 0.50$ and $\theta = 90^\circ$. (Reproduced from Kang et al. [60].)

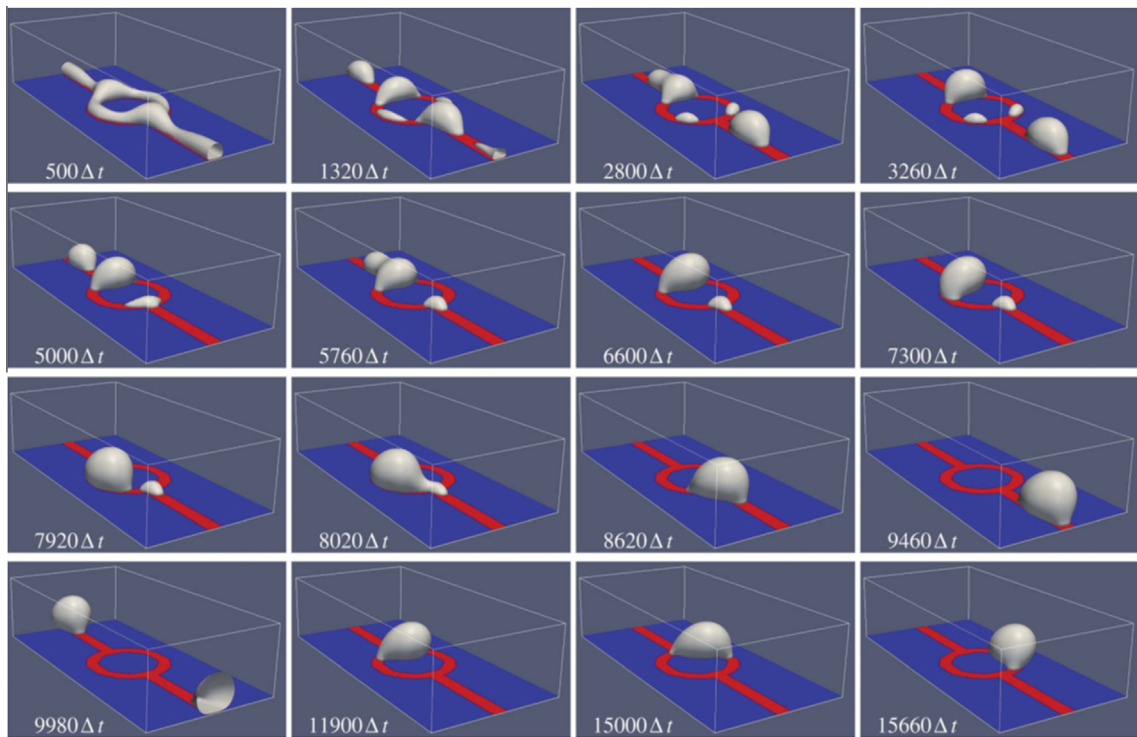


Fig. 9. The dynamic behaviors of water on a symmetric pattern with hydrophilic channel (Red) on a hydrophobic substrate (blue). The stable directional motion of the liquid droplet along the hydrophilic channel can be clearly observed when $t > 9460\Delta t$. (Reproduced from Dörfler et al. [68].) (For interpretation of the references to color in this figure legend, the reader is referred to the web version of this article.)

non-uniform bulges or pearls could be generated due to the hydrodynamic instability. Fig. 9 shows the dynamic behaviors of water on a symmetric pattern with hydrophilic channel (red part) on a hydrophobic substrate (blue part). As can be seen from the figure, after the instability in the initial stage, the stable directional motion of the liquid droplet along the hydrophilic channel can be obtained ($t > 9460\Delta t$).

7.1.2. Impingement of liquid droplets onto a dry surface

Impingement of liquid droplets onto a dry surface is commonly encountered in many natural processes as well as many industrial applications such as rain drops on the surface of the earth, ink-jet printing and spray cooling. Several parameters affect the droplet behaviors including the solid surface wettability and roughness, impact velocity, droplet size, physical properties of the droplet and the surrounding gas, as well as the impact angle [69,70]. Various behaviors such as deposition, splashing, breaking-up and rebounding can be observed depending on the impact conditions. The important dimensionless numbers are the Weber number We (the ratio of inertia force to surface tension force) and the Reynolds number Re (the ratio of inertia force to viscous force). The pseudopotential model was applied to simulate the impingement of a liquid droplet on a dry surface for different We and Re [69,70]. Further, Hyväloma and Timonen [71] studied the droplet impact on a super-hydrophobic surfaces consisting of an array of micron-scale posts.

7.1.3. Superhydrophobic surface

Super-hydrophobic surface has drawn much due to its potential applications such as pressure drop reduction and self-cleaning function. The hydrophobic characteristics of a surface can be enhanced by chemical surface modification. It can be further enhanced by modifying the surface microstructures. Almost all the solid surfaces are naturally rough at the micro/nano-scale.

The rough characteristics can profoundly affect the wettability property of the solid surface. At least two states have been found to describe the droplet on rough surface. One is the Wenzel state in which the droplet penetrates into the rough grooves and wets the surface beneath it. Another is the Cassie's state in which the droplet resides on the top of the groove tips trapping gas in the groove. Cui et al. [76] adopted the MCMP pseudopotential model to investigate fluid flows through channels with different wettability and topographical surfaces. It was found that the super-hydrophobic rough surface reduces the contact area between liquid water and the solid surface and greatly reduces the flow friction. In addition, Zhang et al. [77] adopted the MCMP pseudopotential model to investigate the wettability phenomena of droplets on a rough solid surface with hierarchical structures constructed of micro-pillars covered with nano-pillars. The transition between the Wenzel and Cassie states for different hierarchical structures was investigated in detail and it was found that the Wenzel-to-Cassie state transition can be promoted by decreasing the fluid-solid attraction, increasing the micro-pillar spacing, or coating the microstructures with nanostructures [77]. Sliding behaviors of the droplet on the rough solid surface was also investigated and pinning of the droplet was observed for micro-pillars with gaps above certain width. Besides, Moradi [78] studied the behavior of small droplets on substrates with both regular and arbitrary rough elements. Different wetting morphologies on the rough solid phases were investigated and the effects of the initial droplet position, droplet volume and the surface geometry on the wetting behaviors were explored.

7.1.4. Highly controlled formation of droplets

Highly controlled formation of droplets is another important issue due to its biological and chemical application. There are several types of micro-fluidic devices for generating the droplets, among which the T-shaped channel is one of the most useful ones

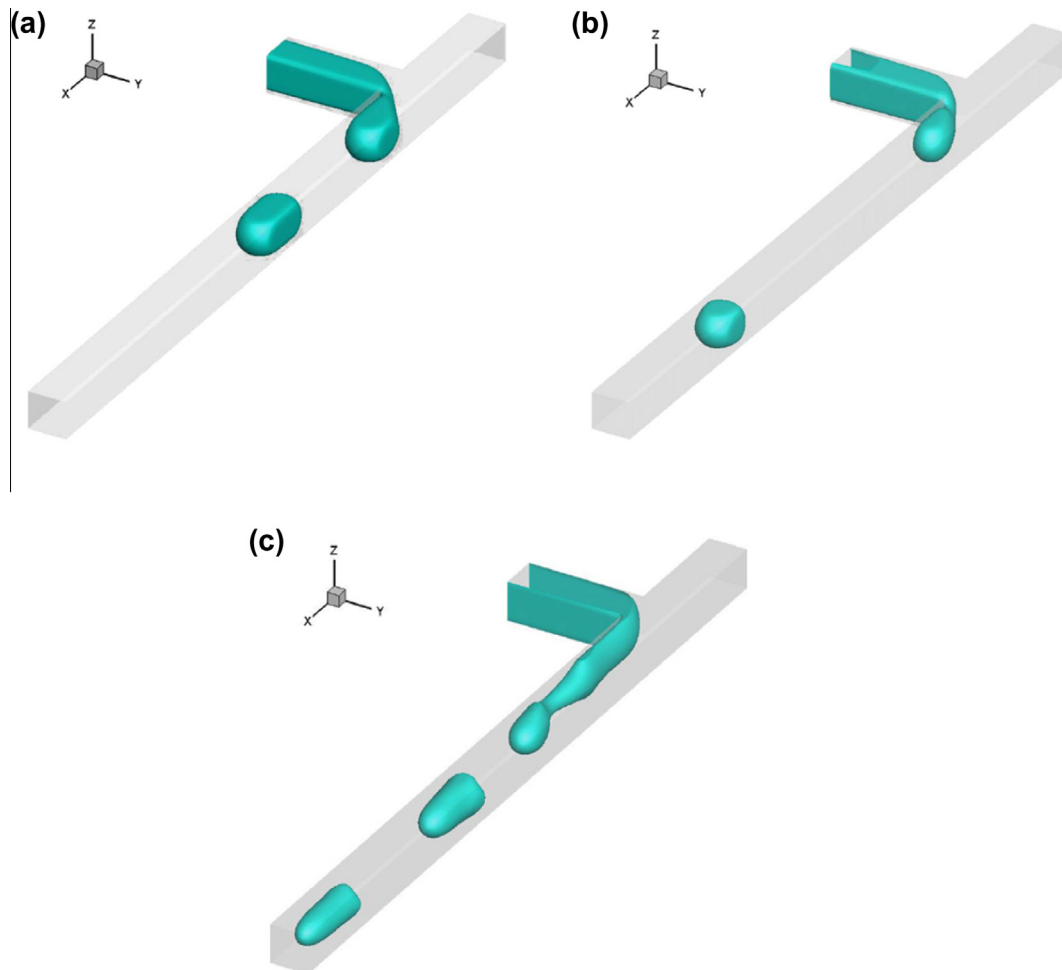


Fig. 10. Three regimes of droplet formation in the T-shaped channel: (a) squeezing regime, (b) dripping regime and (c) the jetting regime. (Reproduced from Yang et al. [74].)

[72–75]. In the T-shaped channel, the flow of the continuous phase cuts the dispersed phase into micro-droplets. Increasing the flow rate of the continuous phase can reduce the size of the micro-droplets. In-depth understanding of the dynamics of the formation of the mono-dispersed droplet and associated single droplet reactor performance is very important. The MCMP pseudopotential model was applied to simulate the droplet formation process in a T-shape micro channel with different configurations on the top of the droplet inlet [73]. Yang et al. [74] adopted the MCMP pseudopotential model to study the droplet formation in a 3D T-shape micro channel. Three regimes of droplet formation were identified including the squeezing regime, dripping regime and the jetting regime (see Fig. 10), and the pressure variations in the dispersed phase and the continuous phase were discussed in detail. Recently, Zhao et al. [75] further extended the work in [73] to study the mixing phenomena inside the droplets.

7.1.5. Droplets suspended in another immiscible fluid

The behaviors of droplets suspended in another immiscible fluid have stimulated much research because of both fundamental and practical interest. Xi and Duncan [93] applied the MCMP pseudopotential model to study the deformation of a single droplet under shear flow. The simulation results for small droplets were in good agreement with Taylor's theoretical results which state a linear relationship between the deformation of the droplet and the Ca . The behaviors of a relative large droplet including deformation stretch and pinching breakup were well captured by the

pseudopotential model. Further, the problem of binary droplet collisions were studied in [94,95], which are of fundamental importance across different scientific problems from understanding raindrop formation in climate theory to engineering applications such as turbine blade cooling. Manaco et al. [94] simulated the collision of two equally sized micro-droplets using the MCMP pseudopotential model. In their simulations, combined techniques of adopting C-S EOS for the liquid component, MRT, and up to 10 isotropic order of the inter-particle force E10 were adopted. The density ratio between liquid phase and gas phase is about 150. A wide range of We and Re were covered and a broad regimes of the collision patterns were captured. Fig. 11 shows the off-center collision processes of two micro-droplets at $We = 140$, $Re = 312.8$ and $B = 0.71$, where B is the normalized distance.

7.1.6. Bubble rising in a stagnant liquid under buoyancy force

Bubble rising in a stagnant liquid under effects of gravitational force is one of the most common gas–liquid flow phenomena. Understanding such a phenomenon is of great importance for the design and operation of industrial applications such as gas–liquid column reactors. The relevant important dimensionless numbers are Bo (Note that Eötvös number Eo can be considered the same as Bo), Mo (the ratio of the viscous force to the surface tension force), and Re number. Depending on different dimensionless numbers, different bubble shapes can be observed including sphere, ellipsoid, spherical cap, skirted shape and dimpled spherical cap. The We number can be constructed as a combination of Re , Mo

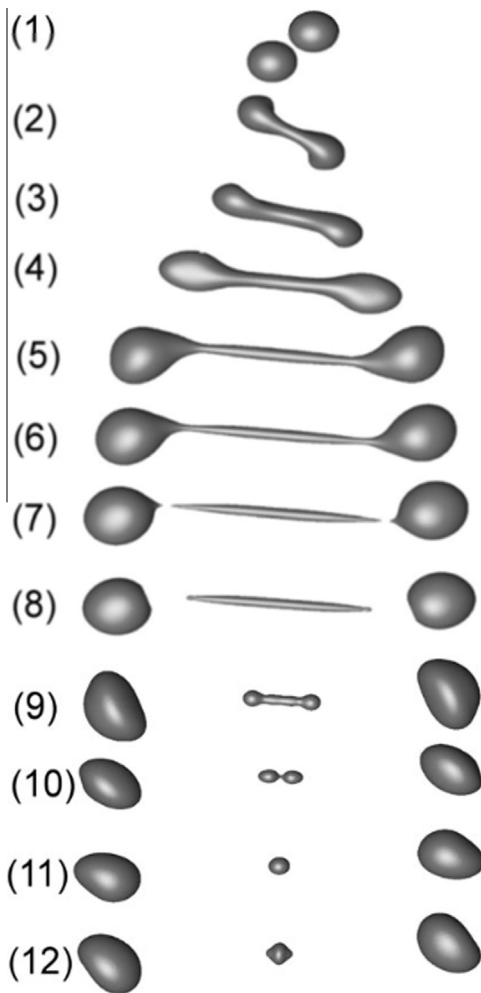


Fig. 11. Off-center collision processes of two microdroplets at $We = 140$, $Re = 312.8$ and $B = 0.71$. (Reproduced from Monaco et al. [94].)

and Bo , namely $We = Re^2(Mo/Bo)^{0.5}$. Liquid–gas systems encountered in nature and industrial systems have Mo ranging from $Mo = 10^{-12}$ (water–air) to $Mo = 10^5$ (syrup–air), and the Bo in the range ($10^{-2}, 10^4$) [35]. Simulation of the bubble rising problem with small Mo and large Bo is challenging as the LBM tends to become numerically unstable at low fluid viscosities [35]. As discussed previously, lower viscosity often leads to larger spurious currents in the pseudopotential model, making the situation worse. Sankaranarayanan et al. [53] adopted the MCMP pseudopotential model to study the dynamics of a rising bubble in liquid with $Bo < 20$ and $Mo > 10^{-6}$ [53]. In their studies, the gas phase was ideal and the liquid phase was a non-ideal component with an artificially constructed EOS. A density ratio of 100 was achieved in their simulations. Later, they improved the numerical model by using an implicit formulation of the LB evolution equation to simulate a wide range of $Bo < 20$ and $Mo > 10^{-10}$ [35], in which the vdW EOS was adopted for the liquid component, and the gas component was treated as ideal gas. The implicit formulation of the LB evolution equation allows for the simulation of low viscosity. In addition, the bubble rising problem was also studied by Gupta and Kumar [89] with Eo in the range of (0.26, 32.18) and Mo in the range of ($3.2 \times 10^{-4}, 3.53 \times 10^{-2}$), in which the original effective mass given by Eq. (10) was adopted for the liquid component, leading to the density ratio only 2.66. Yu et al. [26,36,37] integrated the adaptive mesh refinement (AMR) and the MRT

techniques with the pseudopotential model to investigate the behavior of a single bubble, bubble pairs and bubble swarms under various conditions. The AMR grid technique helps improve the resolution of the bubble interface and enables the pseudopotential model to simulate ellipsoidal cap and skirted bubbles with large deformation. The MRT enhances the pseudopotential model's stability at low viscosities. The behaviors of bubbles with low Mo ($< 10^{-11}$) and high Re ($> 10^3$) were successfully predicted. Finally, it is worth mentioning that because the buoyancy force plays an important role in the behaviors of the bubbles, the introduction of the gravitational force into the pseudopotential model is thus crucial and Eq. (40) should be adopted for the study of bubble rising in a periodic domain without solid walls, as discussed previously. Besides, the simulation can first run without gravitational force for a few thousand steps to let the system equilibrate, and then the gravitational force can be applied. This way the numerical stability can be enhanced [37].

7.2. Slippage phenomena

Recently, micro-electro-mechanical system (MEMS) has drawn extensive attention due to its potential application in chemical, biological and mechanical sciences. Understanding the transport processes in such system is crucial to enhancing its efficiency. One phenomenon of particular interest is the slippage at the solid boundary, which indicates the no-slip boundary condition may no longer hold for flows at micro-/nano-scales. This phenomenon is still far from understanding due to the complex mechanisms and multiple factors involved such as the solid wettability, the pressure gradient, the surface roughness and the impurities and the dissolved gas [96].

There are two common methods in the LB framework for studying the boundary slip [97,98]. One is to allow specular reflections with a given probability at the boundary and the other one is to modify the fluid's viscosity related to the Knudsen number. The pseudopotential model provides an alternative way [57,96,99–104]. Based on the assumption that the formation of a gas layer is the most probable cause of the slippage phenomenon, Zhu et al. [100] introduced forces between solid walls and the fluid particles into the MCMP pseudopotential model, which exponentially decay away from the wall, to study the apparent slip flow on a hydrophobic wall. The force is repulsive to the liquid component and neutral to the gas component. It was found that with such forces the liquid density decreased and the gas density increased close to the wall, and the slip phenomenon was clearly captured. Benzi et al. [57,99] calculated the interaction force between fluid particles and the solid walls using Eq. (47), in which a virtual density is assigned to the solid nodes, thus introducing a mesoscopic force between the walls and the fluid. They simulated fluid flow in a 2D channel using the SCMP pseudopotential model. It was found that with the increase of the hydrophobic property of the solid surface (by decreasing the density of the solid phase from liquid density to the vapor density), the gas layer close to the wall becomes increasingly thicker, and the apparent slip length increases.

Surface roughness effects were also taken into account in [57,102]. The proper treatment of the surface variation in very confined geometries is of great importance for interpretations of flow field [102]. The formation of a gas film in the grooves between rough elements helps increase the slip length and hence decreases the frictions. Further, Hyvälomag et al. [103,104] adopted the SCMP pseudopotential model to study the laminar flow past structured surface with grooves filled with gas bubbles. In the Cassie's wetting state, the droplet resides on the top of the groove tips trapping gas beneath it. Hyvälomag et al. [103,104] investigated the effects of the bubble protrusion angle, the different shapes of

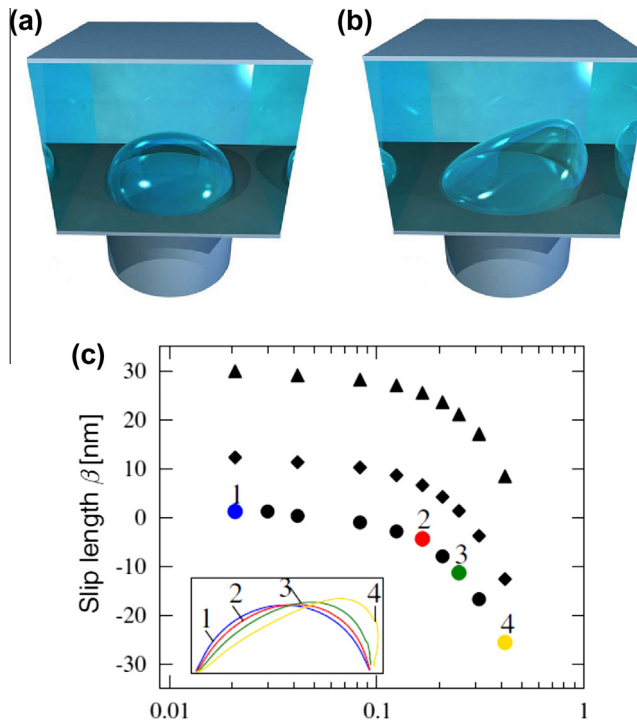


Fig. 12. Snapshots of simulations of bubbles on structured surfaces with Capillary number (a) $Ca = 0.02$ and (b) $Ca = 0.4$. (c) the slip length as a function of the capillary number for a square array of bubbles with three different protrusion angles $\varphi = 63^\circ$, 68° , and 71° (from uppermost to lowermost). The inset shows cross sections of liquid-gas interfaces for four Ca . It can be clearly observed that the slip length decreases as the shear-rate increases. The above simulation results greatly enhance our understanding of the slippage phenomena and will help develop micro-patterned super-hydrophobic surfaces to decrease the flow friction in the microfluidic applications. (Reproduced from Hyväloma and Harting [103].)

roughness elements and shear rate on the slip length. It was found that the bubbles have great effects on the fluid flow in the channel. Even negative slip lengths for flow over the bubbles were obtained under certain conditions. Fig. 12 shows the snapshots of bubbles on structured surfaces with different Ca , as well as the slip length as a function of the Ca for a square array of bubbles with three different protrusion angles $\varphi = 63^\circ$, 68° , and 71° (from uppermost to lowermost). The inset shows cross sections of liquid-gas interfaces for four Ca . It can be clearly observed that the slip length decreases as the shear-rate increases. The above simulation results greatly enhance our understanding of the slippage phenomena and will help develop micro-patterned super-hydrophobic surfaces to decrease the flow friction in the microfluidic applications.

7.3. Multiphase flow in porous media

Multiphase flow in porous media plays an important role in a wide variety of industrial processes such as oil recovery, geological sequestration of CO_2 , underground pollutant remedy and proton exchange membrane fuel cell (PMEFC), and has considerable economic and scientific importance in these practical applications. Due to its easy implementation of phase interaction and the solid wall wettability, the pseudopotential model has been successfully applied to study multiphase flow in porous media at the pore-scale.

The first work of applying the pseudopotential model to multiphase flow in porous media was performed by Martys and Chen in 1996 [45]. In this work, for the first time the fluid–solid interaction was introduced into the pseudopotential model, enabling the model to take into account the surface wettability. The porous medium used was derived from a microtomography image of a Fontainebleau sandstone. Imbibition and drainage processes were

simulated and it was found that the non-wetting phase transports in such a way that it always invades into the largest pores during the drainage process, while the wetting phase mainly transports along the solid surface, leading to considerable amount of non-wetting phase trapped. This study demonstrated that the realistic pore morphology and topology of porous media can be resolved in the LBM. The simulation can provide accurate and fruitful pore-scale information of multiphase flow in porous media such as pore-scale velocity field, detailed phase distributions and complex interfacial areas, all of which are difficult to obtain with the current experimental techniques.

Capillary pressure–saturation curves were predicted using the MCMP pseudopotential model by Pan et al. [105]. They simulated two-phase flow in a porous medium constructed of randomly packed spheres. An efficient parallel LB algorithm was developed to enhance the ability of LB application to porous media with high resolutions [106]. By tuning the physical properties in the LBM according to that in the experimental two-phase displacement processes, hysteretic capillary pressure–saturation relations obtained from the simulation results were found in good agreement with the experimental results. The hysteresis was also found by Sukop and Or [107] who adopted the SCMP pseudopotential model to simulate the liquid–vapor distributions in a porous medium based on 2D imagery of a real soil.

7.3.1. Viscous fingering

Viscous fingering is an important phenomenon in multiphase flow through porous media. In enhanced oil recovery, water or gas is often injected into the well to displace the residual oil. Since the viscosity of the oil is higher than that of water or gas, fingering phenomenon may occur due to the unstable displacement as a result of the viscosity contrast. This fingering phenomenon is undesirable as it reduces the oil recovery efficiency. The pseudopotential model has been successfully applied to study the viscous fingering phenomenon at the pore-scale both in Hele-Shaw cell and in porous media. Chin et al. [108] studied the viscous fingering phenomenon with different viscosity ratios in a 2D channel. Lately, Kang et al. [59] investigated the effects of Ca and wettability on fingering in a simple 2D channel. Dong et al. [109] further emphasized the effects of gravity, who further studied the viscous fingering in a 2D simplified porous medium with solid circles with a staggered arrangement [110]. In all of the above simulations, the density ratio is only 1 and the kinematic viscosity ratio is less than 10. Therefore, further investigation is required for the fingering phenomena under high density ratio and kinematic viscosity ratio. It is worth mentioning that the current 2D investigations completely neglect the effects from the third dimension which are believed to play an important role in the formation of the finger. Thus, further 3D studies should be carried out, although the third dimension has been roughly taken into account using an effective viscous drag force in the 2D model [111].

7.3.2. Relative permeability

Relative permeability is one of the basic parameters required for continuum scale simulations of multiphase flows in porous media. While Darcy's law is widely used for single phase flow in porous media, there is no well-established theory for simultaneous flow of two or more immiscible fluids due to complex fluid–fluid and fluid–solid interactions. A modified form of Darcy's law is commonly used for two-phase flow in porous media, where the relative permeability is introduced. Accurate assessment of the relative permeability is a great challenge as it depends on several factors including the Ca , viscosity ratio, saturation, the solid surface wettability and the interface area between the two fluids [112–117]. Generally, both fluids distribute in most of the flow paths in porous media and viscous coupling between fluids may be strong. The

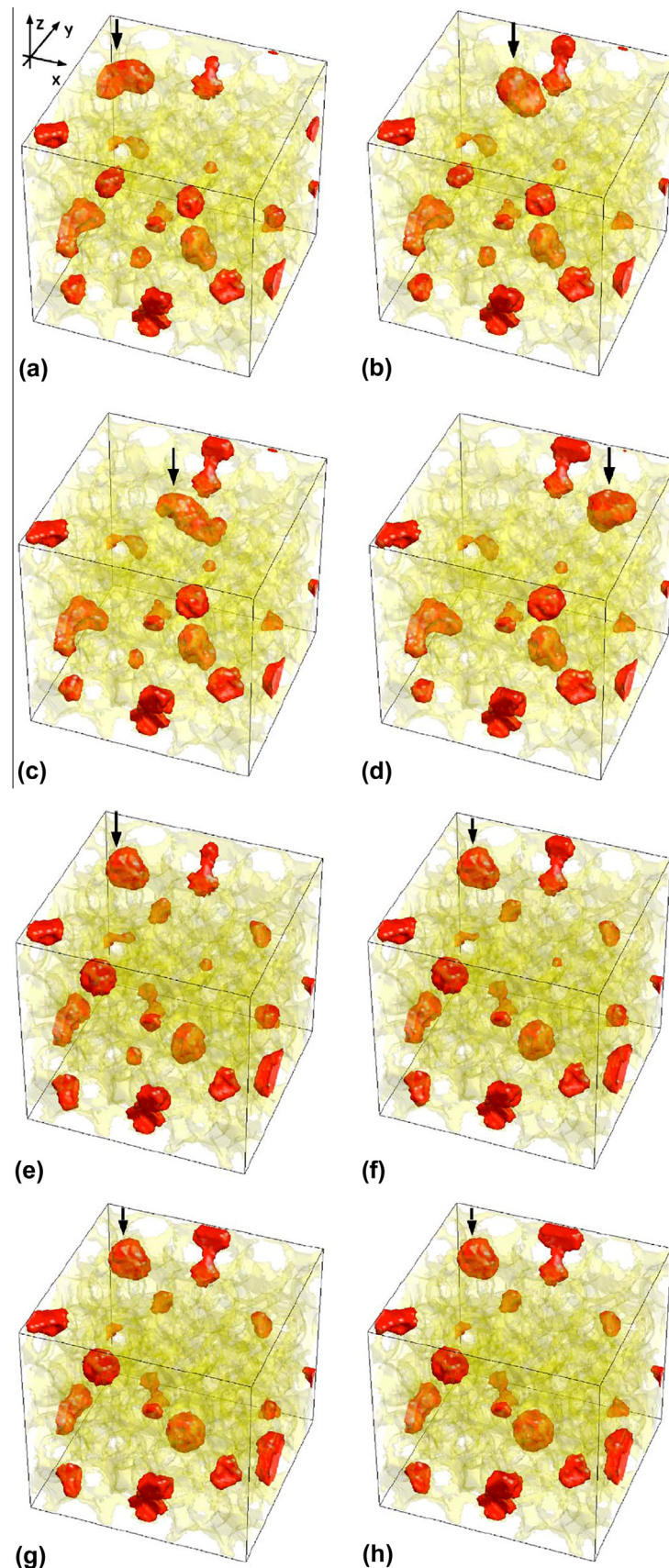


Fig. 13. Snapshots of the non-wetting phase distribution under different capillary number (a–d) $Ca = 5 \times 10^{-4}$ and $Ca = 5 \times 10^{-5}$ (e and f). The NWP region indicated by the arrow in (a–d) moves through the porous medium driven by momentum transferred from the wetting phase at higher Ca , while it is unable to move at lower Ca . (Reproduced from Li et al. [112].)

viscous coupling, which is the driving force of momentum transfer between the two fluids, has great effects on the multiphase flow in porous media and relative permeability. The viscous coupling has been taken account into the modified Darcy's law which includes both diagonal permeability k_{ii} and the off-diagonal permeability k_{ij} , with k_{ij} accounting for viscous coupling. Traditionally, relative permeability is determined by experiments using different measurement methods such as unsteady-state and steady-state methods. However, these measurements are often time consuming and difficult to perform and interpret. Therefore, the data on relative permeability is scarce. Pore-scale simulation provides an alternative tool to predict empirical relations for continuum scale simulations [45]. Li et al. [112] studied the co-current multiphase flow in a 3D porous medium, using body force to drive the flow. Momentum transfer between the wetting phase and the non-wetting phase, namely the viscous coupling phenomenon, was observed under relatively high Ca (Fig. 13). Effects of Ca , wettability and viscosity ratio on the relative permeability were investigated in detail. Complex effects of the wettability on the phase connection and fluid–solid contact were revealed. As the viscosity ratio between the non-wetting phase and the wetting phase increases, the relative permeability of the non-wetting phase greatly increases due to the lubricating effects of thin wetting films covering the solid surfaces, thus facilitating the flow of the non-wetting phase. The comparable conventional relative permeability and the diagonal relative permeability further demonstrated the strong effects of the viscous coupling. Since the viscous coupling is closely related to the interfacial area, the interfacial area also plays a crucial role in the relative permeability.

Effects of the wettability, Ca and viscosity ratio on the relative permeability were also studied by Ghassemi and Pak [113]. In addition, Huang et al. [114,115] adopted the SCMP pseudopotential model to investigate the viscous coupling effects for immiscible two-phase flow in a 2D porous medium, in which higher density ratios were considered compared with previous studies. In their

studies, the density ratio for most of the simulations was 12 and the maximum one was 54. Both concurrent and countercurrent flows were investigated and their effects on two phase distributions and relative permeability were explored. Dou and Zhou [116] further investigated the effects of porous structures on relative permeability by adopting a homogeneous and a heterogeneous porous media. They found that the heterogeneity of the porous media has great effects on the relative permeability and the lubricating phenomenon. In addition, Porter et al. [117] emphasized the importance of the wetting–nonwetting interfacial area. They adopted the MCMP pseudopotential model to study the hysteresis in the relationship of capillary pressure–saturation–interfacial areas in a three-dimensional pore structure of packed glass beds obtained by the computed micro-tomographic (CMT) image technique. The results and discussion of the interfacial area–saturation and pressure–interfacial area–saturation were presented.

7.3.3. Effective diffusivity

Effective diffusivity is another important macroscopic transport parameter of the porous media. In order to evaluate the ionic diffusivity in partially saturated cement-based materials, Zhang et al. [118] incorporated C-S EOS into the SCMP pseudopotential model and simulated the water–vapor distributions with various saturations in a cement-based porous material. The LB diffusion model was subsequently applied to simulate the diffusion process of the ionic species through the partially saturated cement paste [118]. Chen et al. [119] adopted the MCMP model to simulate the liquid water–air distribution in a carbon fiber-based porous medium with mixed wettability. Effects of the wettability on the two-phase distribution and on the effective diffusivity were explored and it was found that when liquid presents as separated films or droplets, the effective diffusivity of the hydrophilic porous medium provides the highest effective diffusivity [119].

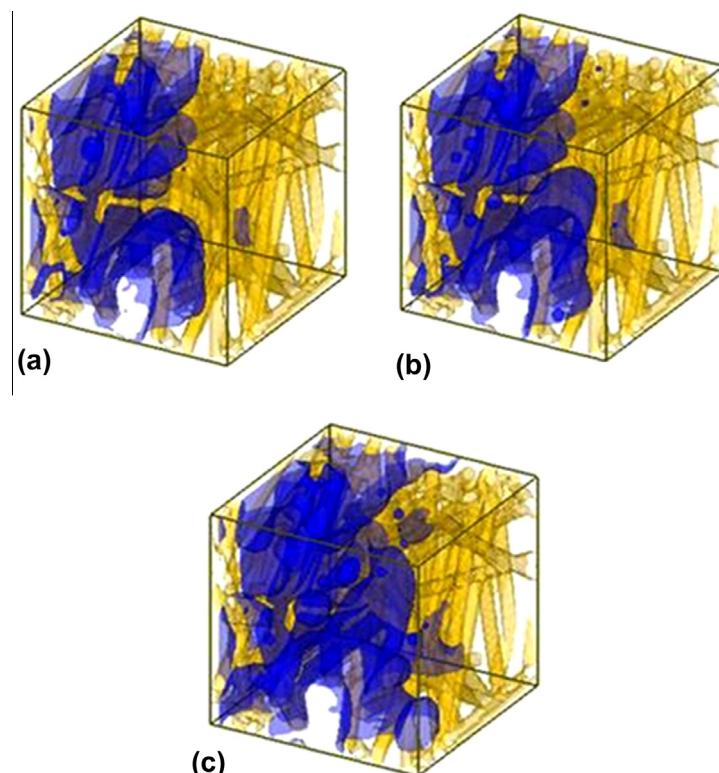


Fig. 14. Capillary fingering of liquid transport through the initially air-saturated reconstructed GDL microstructure. (Reproduced from Mukherjee et al. [25].)

7.3.4. Multiphase flow in proton exchange membrane fuel cell

Another major application of the pseudopotential model is to simulate two phase flows in the gas channel (GC) and porous components (gas diffusion layer (GDL) and catalyst layer (CL)) of PEMFC. PEMFC is a promising candidate of the power source for a range of applications because of its notable advantages such as high power density, high efficiency, low operation temperature, low noise and no pollutions. Successful water management in the PEMFC, particularly in the cathode side, is crucial to the cell performance, as poor water management results in either dehydration of membrane or flooding issues. Flooding problems occur if excessive liquid water accumulates in the components of a PEMFC

including GC, GDL, and CL. Flooding can seriously debilitate cell performance at three different length scales. At the microscopic scale, liquid water fills the micro pores and covers the CL surface, hindering oxygen transport and reducing the reactive surface. At the mesoscopic scale, liquid water clogs pores of GDL, reducing the effective transport of gaseous reactant to the reactive site. At the macroscopic scale, liquid water blocks the GC, resulting in mal-distribution of oxygen and additional pumping power to overcome the increased pressure drop. Therefore, many researchers have highlighted the need for proper water management, and extensive studies have been carried out to investigate liquid water transport processes in the components of a PEMFC [120–125].

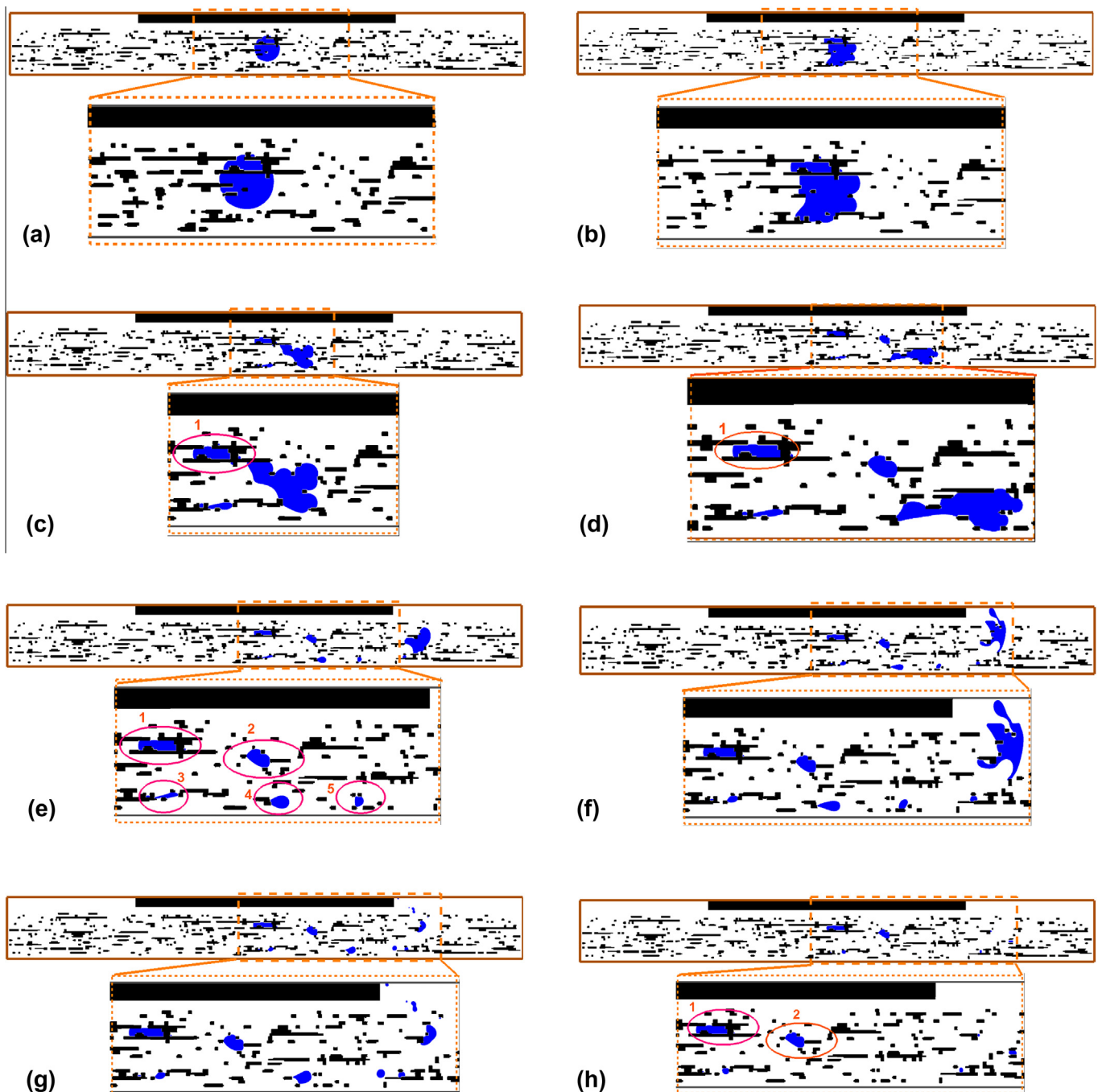


Fig. 15. Pore-scale behaviors of liquid water inside a GDL of interdigitated PEMFC (Black: carbon fibers or land; white: void space; blue: liquid water). 1: $t = 100 \delta t$ (lattice units), 2: $t = 3000 \delta t$, 3: $t = 10000 \delta t$, 4: $t = 28000 \delta t$, 5: $t = 51000 \delta t$, 6: $t = 52000 \delta t$, 7: $t = 54000 \delta t$, 8: $t = 69000 \delta t$. (Reproduced from Chen et al. [130].) (For interpretation of the references to color in this figure legend, the reader is referred to the web version of this article.)

Liquid water transport process in GDL and CL is essentially the transport of liquid water in microscopic porous media with anisotropic structures and mixed wettabilities. The pseudopotential model is the most widely used multiphase model for studying two-phase flow in porous components of PEMFC. Koido et al. [126] simulated the distributions of liquid water in the GDL and predicted the relative permeability. Park and Li [127] investigated the dynamic behaviors of a droplet subjected to a slow air velocity, in which the droplet movement, interaction with the porous structures and break up behaviors were well captured. Mukherjee et al. [25,121] constructed the 3D GDL porous structures and investigated the liquid water invading. They pointed out that the mechanism of liquid water transport in the GDL is capillary fingering as the Ca is of the order of 10^{-6} – 10^{-8} and the viscosity ratio M is about 17.5 in a typical PEMFC. Fig. 14 shows the simulation results of capillary fingering process in the GDL. They also simulated the two-phase distribution in GDL and CL with mixed-wettability. Recently, Gao et al. [128] investigated the effects of the GDL wettability on the liquid water transport. They found out that with an increase in hydrophobicity, water transport in GDL changes from piston-flow to channel flow. Han and Meng [129] also studied the liquid water distribution and transport processes in the GDL with modified porous structures.

While the above studies were mainly devoted to liquid transport in GDL under parallel GC where the air flow rate is extremely small, Chen et al. [130] applied the MCMP pseudopotential model to study the dynamic behaviors of a droplet subjected to relatively strong air flow in a GDL under the interdigitated GC (see Fig. 15). Compared to previous studies mainly focusing on capillary fingering, the dynamic behaviors of the liquid water dominated by viscous force were emphasized. Effects of the air flow velocity and wettability on the removal time and residual saturation of the liquid water in GDL were investigated in detail.

Besides its application in PEMFC, the pseudopotential model was also used to simulate electrolyte transport in a 2D porous electrode structure of lithium-ion batteries in which Re is of the order 10^{-3} and Ca is of the order of 10^{-5} [131]. Thus the transport process of electrolyte in the porous electrode is quite similar to that of liquid water transport in GDL under parallel gas channel of PEMFC. Finally, the pseudopotential model has also been adopted to simulate two-phase flow in GC [132,133].

7.4. Coupling with other methods for complicated multiple physicochemical processes

7.4.1. Coupled with thermal LB model for phase change heat transfer

Nucleation boiling heat transfer is one of the most effective transfer models and has been widely adopted in heat exchangers and nuclear reactors. One of the fundamental phenomena involved in such a heat transfer model is the generation, growth, departure and coalescence of the bubbles. While early studies of the bubble behaviors were modeled by injecting the bubbles into the domain through a nozzle [134], recently the pseudopotential model was coupled with a thermal LB model to study the departure of gas bubbles from a horizontal plate with heterogeneous boiling [135,136] where the bubble generation was spontaneously caused by phase change. The diameter and release frequency of the departure bubbles under different contact angle and body force were investigated in detail [135,136]. While a hypothetic EOS were used in Ref. [135], Gong and Cheng [31] incorporated the P–R EOS into the pseudopotential model which was then coupled with a thermal LB model to study liquid–vapor phase change heat transfer [137]. Effects of gravity, contact angle and superheat on the diameter and release period of the departure bubbles under constant wall temperature conditions were studied. In addition, Biferale et al. [138] presented high-resolution numerical simulations of

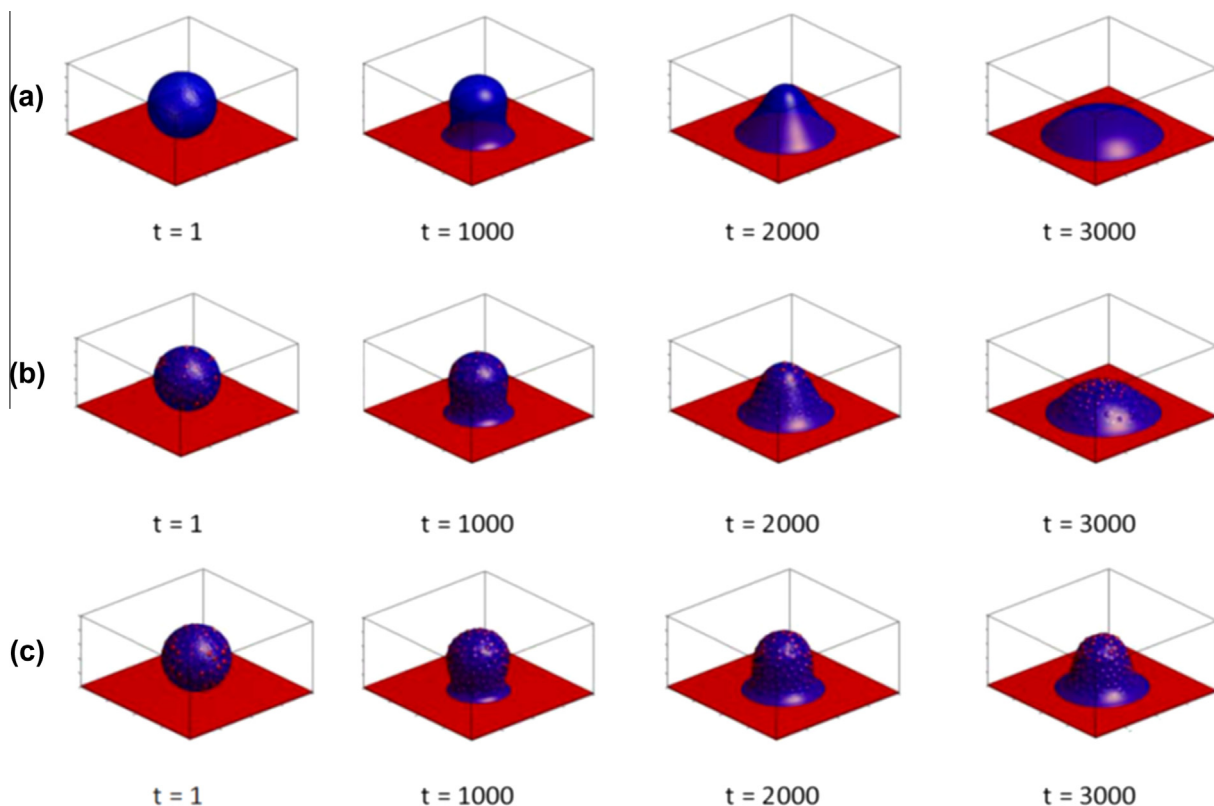


Fig. 16. The spreading dynamics of the droplet on the substrates with different particle volume fraction, (a) pure liquid drop, (b) 15% particle volume fraction and (c) 30% particle volume fraction. (Reproduced from Joshi and Sun [142].)

convection in boiling and demonstrated the thermal and mechanical effects of bubbles on the convective heat transfer in the multiphase flow. Besides, condensation process is another important heat transfer model, and the film-wise and droplet-wise condensation processes were studied in [139,140] by using the same coupled model proposed in [31]. Since conventional multiphase

flow models require droplet or bubble nucleus prescribed in the initial system, the pseudopotential model combined with heat transfer modeling techniques is probably the most promising tool to reveal the nucleation mechanism, a crucial and not well understood scientific question in phase change heat transfer processes. Further work is required to adopting the pseudopotential

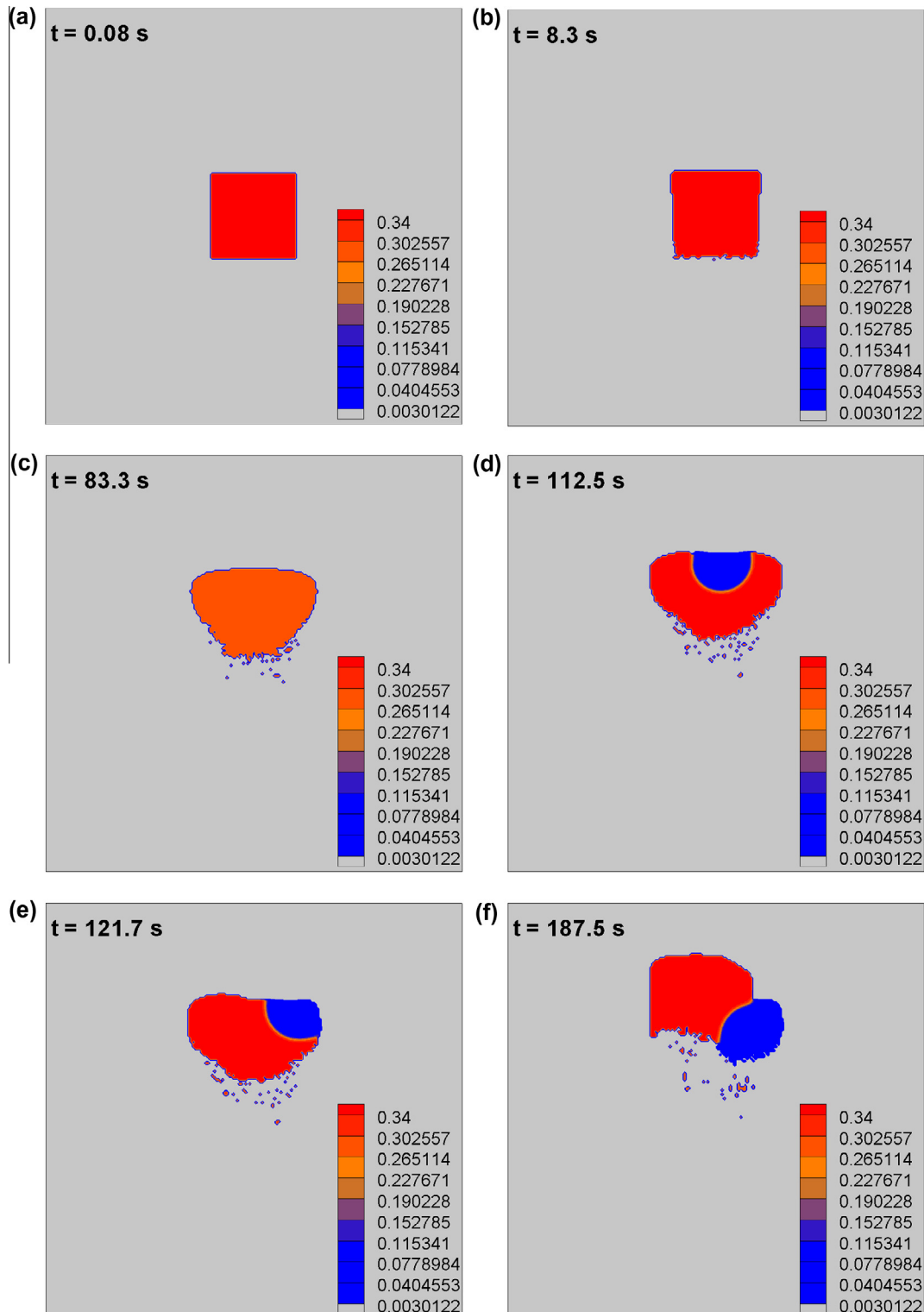


Fig. 17. Simulation results of fluid densities and solid geometries during the thermal migration of a brine inclusion in a single salt crystal. The square located at the center of the domain at $t = 0.08$ s is the inclusion and the remaining part is the solid crystal. The solid phase around the upper part of the inclusion dissolves and the lower part precipitates, leading to the upward migration of the inclusion. (Reproduced from Chen et al. [46].)

model to explore the nucleation mechanism under different temperature boundaries and wall characteristics, and to investigate the complicated effects of the dynamic behaviors of the bubbles or droplets on the physics of fluid flow and the thermodynamics of the phase change heat transfer.

7.4.2. Coupled with particle suspension model for solid particle suspension

Multiphase flow containing colloids are commonly encountered in scientific and engineering areas such as viruses and bacteria transport in air–water flow near the land surface and inkjet print and emulsions [141–146]. Joshi and Sun [141] developed a multiphase suspension model by combining the SCMP pseudopotential model with a particle suspension model for a two-phase system with suspended particles in both phases. The capillary force between the suspended particles and the fluids, which makes the problem more complex compared to the single phase suspension model, was included in their model. They further extended their model to 3D and took the evaporation into account [142]. Note that the evaporation was considered by artificially removing certain amount of vapor from the out boundary rather than using a thermal LB model. The model developed was applied to explore the dynamic wetting behavior of drops containing suspended solid particles on homogeneous and patterned substrates. Fig. 16 shows the spreading dynamics of a droplet on the substrates with different particle volume fractions. It can be observed that the particles significantly slow the spreading of the droplet on the substrate as they increase the effective viscosity of the droplets. In addition, Jansen and Harting [143] also coupled the MCMP pseudopotential model with a suspended particle model which can simulate particles with variable contact angle in multi-component fluid flows. Effects of the contact angle of the particles, the particle numbers and the density ratio of the multiphase fluid on the transition from Bijel to Pickering emulsion were explored. Frijters et al. [144] further extended the work of Jansen and Harting [143] to study the effects of nano-particles and surfactant on droplet in shear flow. Compared with previous work about multiphase suspension with extremely slow fluid flow, a droplet subjected to shear flow was considered. Deformation of the droplet, inclination angle relative to the shear flow, the dynamics of the particles at the interface, and the possibility of breakup were investigated [144]. Recently, Krüger et al. [145] presented a review of their work about combining the pseudopotential model and the suspension particle model for multiphase system involving particles.

7.4.3. Coupled with mass transport model for multiphase reactive transport process

In geology, the multiphase fluid flow is often coupled with several other physicochemical processes including heat transfer, transport of multiple species, homogeneous reaction in the bulk fluid and heterogeneous reactions at the fluid–solid interface, as well as dissolution (melting) and precipitation (solidification) of the solid phases. The required model not only should be capable of dealing with the multiphase flow dynamics, but also can simulate the heat transfer and species transport as well as can considering the dynamic evolution of the fluid–solid interfaces [46].

Recently, by combining the SCMP pseudopotential model with a mass transport LB model and a solid–liquid interface tracking model, Chen et al. [46] proposed a pore-scale model for multiphase reactive transport with phase transition and dissolution/precipitation. They carefully handled the fluid flow and mass transport information on computational nodes undergoing solid/liquid or liquid/vapor phase changes to guarantee mass and momentum conservation. The pore-scale model can capture coupled non-linear multiple physicochemical processes including multiphase flow with phase separation, mass transport, chemical reaction,

dissolution–precipitation, and dynamic evolution of the pore geometries. The model was used to study the thermal migration of a brine inclusion in a salt crystal encountered in nucleation waste treatment industry. Fig. 17 shows the thermal migration of an inclusion in a solid crystal. Subjected to the temperature gradient, the solute concentration at the bottom of the inclusion is super-saturated, while that at the top of the inclusion is undersaturated. Therefore, the salt precipitates at the bottom of the inclusion (cold sites) and dissolves at the top of the inclusion (hot sites). Such a micro evolution of the geometry leads to the macro observable migration of the inclusion. It can be seen in Fig. 17 that the macro thermal migration of the inclusion, as well as the microscopic coupled multiple physicochemical processes (multiphase flow with phase separation, mass transport, surface reaction, and dissolution/precipitation) were all well captured by the pore-scale model.

Very Recently, Chen et al. further proposed a multi-phase multi-mixture model for multi-component multiphase reactive transport processes, where the MCMP model was used to establish the liquid–gas two fluid phase system [63]. The model was used to simulate a physicochemical system involving liquid–gas two phases, five components, two solid phases and four reactions including decomposition, dissolution and precipitation reactions. The complex interactions between different sub-processes were investigated and discussed in detail. Besides, MCMP pseudopotential model was also coupled with a thermal LB model to simulate the multiphase flow with melting and solidification of the solid phase in [147].

8. Conclusion and discussion

There have been several multiphase models in the community of multiphase flow. Those models based on the traditional CFD can be divided into two main categories, namely the front-tracking and the front-capturing models. The front-tracking (such as Boundary Element Method: BEM) and front-capturing (Such as Volume of Fluid (VOF) and Level Set Method (LS)) models require artificial interface reconstruction techniques in which dedicate treatments are implemented near the phase interface. In the LB framework, there also have been several multiphase flow models also employing the tracking/capturing techniques such as the RK multiphase model [2,148]. In contrast, the pseudopotential multiphase LB model incorporates the microscopic molecular interactions, which is the physical origin of interfacial behaviors of multiphase flow. Hence, the phase interface is no longer a mathematical boundary and explicit interface-tracking or interface-capturing technique is not needed. The phase interface is a post-processed quantity that can be detected through monitoring the variation of the fluid densities. This physics-originated rather than phenomenological characteristic is a significant distinction between the pseudopotential model and most of other multiphase models. Such physics-based characteristics results in several benefits. From the view point of computational implementation, it means desirable modeling convenience and notable computational resource saving. From the point view of application, it empowers the pseudopotential model to study a class of super-molecular multiphase flow as called in [27], in which the continuum assumption does not strictly stand while a complete atomistic description is still not necessary. Multiphase flows in microfluidics and nanofluidics are typical examples, where surface tension and fluid–solid interactions begin to dominate the dynamic behaviors and distributions of multiphase fluid [15,149], and slippage phenomena emerge at the wall [99,101]. The flexibility of introducing mid-range repulsion force which generates positive disjoining pressure further enables the pseduopotential model to capture an entirely new set of physical regimes including atomization, spray

formation, micro-emulsions and soft-glassy system [47–51]. Based on this review, it is reasonable to conclude that the pseudopotential model has exhibited outstanding advantages for fruitful applications, and have demonstrated crucial roles for exploring super-molecular multiphase flow.

Obviously, further widespread applications of the pseudopotential model require the removing/relaxing of its limitations including the relatively large spurious currents, thermodynamic inconsistency, the limited density and kinetic viscosity ratio, the interdependence between the EOS and surface tension, and the dependence of surface tension and density ratio on the viscosity. Currently, the last two limitations have been basically resolved. Sbragaglia et al. [27] demonstrated that by taking into account the mid-range potential, the surface tension can be adjusted independently. The dependence of surface tension and density ratio on viscosity can be unraveled by using proper force scheme [32] and by using MRT [26].

However, the relatively large spurious current still require further effort. Recently, Scarbolo et al. [150] developed a unified framework for a side-by-side comparison of the pseudopotential model with free energy LB multiphase model (another physics-originated model in the LB framework which is thermodynamically consistent [8]) and phase field method. It was found that the pseudopotential model and free energy model behave similarly. The spurious currents in pseudopotential model are two magnitudes stronger than that of phase field method, which also are far higher than that of the multiphase model proposed by Lee and Fischer [151]. Employing Lee and Fischer's model, the spurious current can be reduced to machine precision [151]. Note that in Ref. [150] the effective mass used is density itself, using effective mass derived from the real EOS in pseudopotential model can greatly reduce the spurious currents [22], and other techniques such as using proper force scheme and MRT are also helpful (discussed in Section 4). Nevertheless, further minimizing spurious currents in pseudopotential model is still urgently required, given the expected widespread applications of the pseudopotential model to the microfluidic and nanofluidic devices where low Re fluid flows are dominant.

In addition, thermodynamic inconsistency, which is an inherent limitation, still incurs extensive criticisms on the theoretical foundations of this model, compared with the free energy LB multiphase model which is thermodynamic consistent [8]. While this issue is relaxed to some extent for the SCMP [24], fundamental analysis and significant improvement is required for the MCMP with large density ratio. In fact, while MCMP with large density ratio is commonly encountered, only until recently there have been a few studies devoted to this topic [36,37,39,40]. In these studies [36,37,39,40], several parameters are casually adjusted by trial and error to achieve the objective density ratio with the lack of physical meaning. Recently, the pseudopotential model has been considered to be the most promising multiphase model to investigate the nucleation mechanism, a crucial and key scientific problem in the phase change heat transfer such as boiling and condensation [135,136,138–140]. This problem cannot be simulated using conventional multiphase models based on phenomenological description of the phase interface, and is also challenging for some multiphase LB models such as the color model or mean-field model. Therefore, enhancing the thermodynamic consistency of the pseudopotential model is crucial for better predicting the bubble (droplet) nucleation process under different conditions (e.g., temperature boundary conditions, wall characteristics, and existence of impurities), and for quantitatively assessing the effects of the dynamic behaviors of the bubbles (droplets) on the thermodynamics of the phase change heat transfer.

Finally, the density and kinetic viscosity ratio should also be increased to expand applications of the pseudopotential model.

Incorporation of realistic EOS significantly is an efficient way for high density ratio [22]. In fact, the ability of incorporating of realistic EOS is a great advantage of the pseudopotential model compared with other multiphase models based on phenomenological description of the phase interface. Nevertheless, while for stationary or quasi-stationary multiphase system density ratio of O(1000) is achieved [22,28,40], it is significantly reduced when fluid flow is relatively strong [39,61]. In addition, large viscosity ratio is another important aspect required for improvement [152]. Currently, the robustness and stability of the pseudopotential model, especially when it is applied to real industrial problems, for example, high Re fluid flow, still need to be improved.

Conflict of interest

We declare that we have no financial and personal relationships with other people or organizations that can inappropriately influence our work, and there is no professional or other personal interest of any nature or kind in any product, service and/or company that could be construed as influencing the position presented in, or the review of, the manuscript entitled.

Acknowledgments

Financial support of this work was provided by the National Nature Science Foundation of China (No. 51136004), the LANL LDRD Program, and the UC Lab Fees Research Program. We thank Dr. Xiaowen Shan for the insightful comments, which have greatly improved the quality of this paper. We also appreciate the useful discussions with Prof. Haibo Huang from University of Science and Technology of China, Research Engineer Jie Bao from Pacific Northwest National Laboratory, Dr. Zhao Yu from the Dow Chemical Company, Dr. Qing Li from University of Southampton, and Prof. M. Sbragaglia from University of Tor Vergata.

References

- [1] S.Y. Chen, G.D. Doolen, Lattice Boltzmann methode for fluid flows, *Annu. Rev. Fluid Mech.* 30 (1998) 329–364.
- [2] A.K. Gunstensen, D.H. Rothman, S. Zaleski, G. Zanetti, Lattice Boltzmann model of immiscible fluids, *Phys. Rev. A* 43 (8) (1991) 4320–4327.
- [3] D. Rothman, J. Keller, Immiscible cellular-automation fluids, *J. Stat. Phys.* 52 (3–4) (1988) 1119–1127.
- [4] X. Shan, H. Chen, Lattice Boltzmann model for simulating flows with multiple phases and components, *Phys. Rev. E* 47 (1993) 1815–1819.
- [5] X. Shan, H. Chen, Simulation of nonideal gases and liquid–gas phase transitions by the lattice Boltzmann equation, *Phys. Rev. E* 49 (4) (1994) 2941–2948.
- [6] X. Shan, G. Doolen, Multicomponent lattice-Boltzmann model with interparticle interaction, *J. Stat. Phys.* 81 (1995) 379–393.
- [7] X. Shan, H. Chen, Diffusion in a multicomponent lattice Boltzmann equation model, *Phys. Rev. E* 47 (1996) 3614–3620.
- [8] M.R. Swift, E. Orlandini, W.R. Osborn, J.M. Yeomans, Lattice Boltzmann simulations of liquid–gas and binary fluid systems, *Phys. Rev. E* 54 (5) (1996) 5041–5052.
- [9] X. He, X. Shan, G.D. Doolen, Discrete Boltzmann equation model for nonideal gases, *Phys. Rev. E* 57 (1) (1998) R13–R16.
- [10] R. Benzi, S. Succi, M. Vergassola, The lattice Boltzmann equation: theory and applications, *Phys. Rep.* 222 (3) (1992) 145–197.
- [11] S. Succi, *The Lattice Boltzmann Equation: For Fluid Dynamics and Beyond*, Oxford University Press, Oxford, 2001.
- [12] D.A. Wolf-Gladrow, *Lattice-Gas Cellular Automata and Lattice Boltzmann Models – An Introduction*, Springer, Berlin, 2000.
- [13] M.C. Sukop, D.T.J. Thorne, *Lattice Boltzmann Modeling: An Introduction for Geoscientists and Engineers*, Springer Publishing Company, New York, 2006.
- [14] C.K. Aidun, J.R. Clausen, Lattice-Boltzmann method for complex flows, *Annu. Rev. Fluid Mech.* 42 (439–472) (2010).
- [15] J. Zhang, Lattice Boltzmann method for microfluidics: models and applications, *Microfluid Nanofluid* 10 (2011) 1–28.
- [16] X. He, L.-S. Luo, Theory of the lattice Boltzmann method: from the Boltzmann equation to the lattice Boltzmann equation, *Phys. Rev. E* 56 (6) (1997) 6811–6817.

- [17] P.L. Bhatnagar, E.P. Gross, M. Krook, A model for collision processes in gases. I. Small amplitude processes in charged and neutral one-component systems, *Phys. Rev.* 94 (3) (1954) 511–525.
- [18] X. Shan, Pressure tensor calculation in a class of nonideal gas lattice Boltzmann models, *Phys. Rev. E* 77 (6) (2008) 066702.
- [19] M. Sbragaglia, H. Chen, X. Shan, S. Succi, Continuum free-energy formulation for a class of lattice Boltzmann multiphase models, *EPL* 86 (2009) 24005.
- [20] M. Sbragaglia, K. Sugiyama, L. Biferale, Wetting failure and contact line dynamics in a Couette flow, *J. Fluid Mech.* 614 (2008) 471–493.
- [21] S. Hou, X. Shan, Q. Zou, G.D. Doolen, W.E. Soll, Evaluation of two lattice Boltzmann models for multiphase flows, *J. Comput. Phys.* 138 (2) (1997) 695–713.
- [22] P. Yuan, L. Schaefer, Equations of state in a lattice Boltzmann model, *Phys. Fluids* 18 (4) (2006) 042101–042111.
- [23] H.B. Callen, *Thermodynamics and An Introduction to Thermostatistics*, second ed., Wiley, New York, 1985.
- [24] M. Sbragaglia, X. Shan, Consistent pseudopotential interactions in lattice Boltzmann models, *Phys. Rev. E* 84 (3) (2011) 036703.
- [25] P.P. Mukherjee, C.-Y. Wang, Q. Kang, Mesoscopic modeling of two-phase behavior and flooding phenomena in polymer electrolyte fuel cells, *Electrochim. Acta* 54 (27) (2009) 6861–6875.
- [26] Z. Yu, L.-S. Fan, Multirelaxation-time interaction-potential-based lattice Boltzmann model for two-phase flow, *Phys. Rev. E* 82 (4) (2010) 046708.
- [27] M. Sbragaglia, R. Benzi, L. Biferale, S. Succi, K. Sugiyama, F. Toschi, Generalized lattice Boltzmann method with multirange pseudopotential, *Phys. Rev. E* 75 (2) (2007) 026702.
- [28] A.L. Kupershmidt, D.A. Medvedev, D.I. Karpov, On equations of state in a lattice Boltzmann method, *Comput. Math. Appl.* 58 (5) (2009) 965–974.
- [29] J. Zhang, F. Tian, A bottom-up approach to non-ideal fluids in the lattice Boltzmann method, *EPL* 81 (2008) 66005.
- [30] X. Shan, Analysis and reduction of the spurious current in a class of multiphase lattice Boltzmann models, *Phys. Rev. E* 73 (4) (2006) 047701.
- [31] S. Gong, P. Cheng, Numerical investigation of droplet motion and coalescence by an improved lattice Boltzmann model for phase transitions and multiphase flows, *Comput. Fluids* 53 (2012) 93–104.
- [32] H. Huang, M. Krafczyk, X. Lu, Forcing term in single-phase and Shan-Chen-type multiphase lattice Boltzmann models, *Phys. Rev. E* 84 (4) (2011) 046710.
- [33] Q. Li, K.H. Luo, X.J. Li, Forcing scheme in pseudopotential lattice Boltzmann model for multiphase flows, *Phys. Rev. E* 86 (1) (2012) 016709.
- [34] K. Sun, T. Wang, M. Jia, G. Xiao, Evaluation of force implementation in pseudopotential-based multiphase lattice Boltzmann models, *Physica A* 391 (15) (2012) 3895–3907.
- [35] K. Sankaranarayanan, X. Shan, I.G. Kevrekidis, S. Sundaresan, Analysis of drag and virtual mass forces in bubbly suspensions using an implicit formulation of the lattice Boltzmann method, *J. Fluid Mech.* 452 (2002) 61–96.
- [36] Z. Yu, L.-S. Fan, An interaction potential based lattice Boltzmann method with adaptive mesh refinement (AMR) for two-phase flow simulation, *J. Comput. Phys.* 228 (17) (2009) 6456–6478.
- [37] Z. Yu, H. Yang, L.-S. Fan, Numerical simulation of bubble interactions using an adaptive lattice Boltzmann method, *Chem. Eng. Sci.* 66 (14) (2011) 3441–3451.
- [38] M.R. Kamali, S. Sundaresan, H.E.A. Van den Akker, J.J.J. Gillissen, A multi-component two-phase lattice Boltzmann method applied to a 1-D Fischer-Tropsch reactor, *Chem. Eng. J.* 207–208 (2012) 587–595.
- [39] M.R. Kamali, H.E.A. Van den Akker, Simulating gas–liquid flows by means of a pseudopotential lattice Boltzmann method, *Ind. Eng. Chem. Res.* (2013).
- [40] J. Bao, L. Schaefer, Lattice Boltzmann equation model for multi-component multi-phase flow with high density ratios, *Appl. Math. Model.* 37 (4) (2013) 1860–1871.
- [41] A. Márkus, G. Házi, Determination of the pseudopotential gradient in multiphase lattice Boltzmann models, *Phys. Fluids* 20 (2) (2008) 022101.
- [42] Q. Li, K.H. Luo, X.J. Li, Lattice Boltzmann modeling of multiphase flows at large density ratio with an improved pseudopotential model, *Phys. Rev. E* 87 (2013) 053301.
- [43] R.S. Qin, Mesoscopic interparticle potentials in the lattice Boltzmann equation for multiphase fluids, *Phys. Rev. E* 73 (6) (2006) 066703.
- [44] Q. Kang, D. Zhang, S. Chen, Displacement of a two-dimensional immiscible droplet in a channel, *Phys. Fluids* 14 (9) (2002) 3203–3214.
- [45] N.S. Marty, H. Chen, Simulation of multicomponent fluids in complex three-dimensional geometries by the lattice Boltzmann method, *Phys. Rev. E* 53 (1) (1996) 743–750.
- [46] L. Chen, Q. Kang, B.A. Robinson, Y.-L. He, W.-Q. Tao, Pore-scale modeling of multiphase reactive transport with phase transitions and dissolution-precipitation processes in closed systems, *Phys. Rev. E* 87 (4) (2013) 043306.
- [47] S. Chibbaro, G. Falucci, G. Chiatti, H. Chen, X. Shan, S. Succi, Lattice Boltzmann models for nonideal fluids with arrested phase-separation, *Phys. Rev. E* 77 (3) (2008) 036705.
- [48] M. Sbragaglia, R. Benzi, M. Bernaschi, S. Succi, The emergence of supramolecular forces from lattice kinetic models of non-ideal fluids: applications to the rheology of soft glassy materials, *Soft Matter* 8 (2012) 10773–10782.
- [49] R. Benzi, S. Chibbaro, S. Succi, Mesoscopic lattice Boltzmann modeling of flowing soft systems, *Phys. Rev. Lett.* 102 (2) (2009) 026002.
- [50] R. Benzi, M. Sbragaglia, S. Succi, M. Bernaschi, S. Chibbaro, Mesoscopic lattice Boltzmann modeling of soft-glassy systems: Theory and simulations, *J. Chem. Phys.* 131 (2009) 104903.
- [51] M. Bernaschi, L. Rossi, R. Benzi, M. Sbragaglia, S. Succi, Graphics processing unit implementation of lattice Boltzmann models for flowing soft systems, *Phys. Rev. E* 80 (6) (2009) 066707.
- [52] L. Amaya-Bower, T. Lee, Single bubble rising dynamics for moderate Reynolds number using lattice Boltzmann method, *Comput. Fluids* 39 (2010) 1191–1207.
- [53] K. Sankaranarayanan, X. Shan, I.G. Kevrekidis, S. Sundaresan, Bubble flow simulations with the lattice Boltzmann method, *Chem. Eng. Sci.* 54 (21) (1999) 4817–4823.
- [54] Z. Guo, C. Zheng, B. Shi, Discrete lattice effects on the forcing term in the lattice Boltzmann method, *Phys. Rev. E* 65 (4) (2002) 046308.
- [55] A.J.C. Ladd, R. Verberg, Lattice-Boltzmann simulations of particle-fluid suspensions, *J. Stat. Phys.* 104 (5–6) (2001) 1191–1251.
- [56] L.-S. Luo, Unified theory of lattice Boltzmann models for non-ideal gases, *Phys. Rev. Lett.* 81 (8) (1998) 1618–1621.
- [57] M. Sbragaglia, R. Benzi, L. Biferale, S. Succi, F. Toschi, Surface roughness-hydrophobicity coupling in microchannel and nanochannel flows, *Phys. Rev. Lett.* 97 (20) (2006) 204503.
- [58] H. Huang, D. Thorne, M.G. Schaa, M.C. Sukop, Proposed approximation for contact angles in Shan-and-Chen-type multicomponent multiphase lattice Boltzmann models, *Phys. Rev. E* 76 (6) (2007) 66701.
- [59] Q. Kang, D. Zhang, S. Chen, Immiscible displacement in a channel: simulations of fingering in two dimensions, *Adv. Water Res.* 27 (2004) 13–22.
- [60] Q. Kang, D. Zhang, S. Chen, Displacement of a three-dimensional immiscible droplet in a duct, *J. Fluid Mech.* 545 (41–66) (2005).
- [61] M. Liu, Z. Yu, T. Wang, J. Wang, L.-S. Fan, A modified pseudopotential for a lattice Boltzmann simulation of bubbly flow, *Chem. Eng. Sci.* 65 (20) (2010) 5615–5623.
- [62] Z. Yu, X. Shan, L.-S. Fan, An improved multi-component lattice Boltzmann method for simulation of gas–liquid flows with high density ratio, in: AIChE Annual Meeting, 2007.
- [63] L. Chen, Q. Kang, Y.-L. He, W.-Q. Tao, Q. Tang, Pore-scale study of multi-component multiphase reactive transport with dissolution and precipitation processes using the lattice Boltzmann method, *Appl. Energy* (submitted for publication).
- [64] M. Sbragaglia, D. Belardinelli, Interaction pressure tensor for a class of multicomponent lattice Boltzmann models, *Phys. Rev. E* 88 (1) (2013) 013306.
- [65] A. Mazloomi, A. Moosavi, Thin liquid film flow over substrates with two topographical features, *Phys. Rev. E* 87 (2) (2013) 022409.
- [66] L. Clime, D. Brassard, T. Veres, Numerical modeling of electrowetting processes in digital microfluidic devices, *Comput. Fluids* 39 (9) (2010) 1510–1515.
- [67] L. Clime, D. Brassard, T. Veres, Numerical modeling of electrowetting transport processes for digital microfluidics, *Microfluid Nanofluid* 8 (2010) 599–608.
- [68] F. Dörfler, M. Rauscher, J. Koplik, J. Harting, S. Dietrich, Micro- and nanoscale fluid flow on chemical channels, *Soft Matter* 8 (2012) 9221–9234.
- [69] A. Gupta, R. Kumar, Two-dimensional lattice Boltzmann model for droplet impingement and breakup in low density ratio liquids, *Commun. Comput. Phys.* 10 (3) (2011) 767–784.
- [70] A. Gupta, R. Kumar, Droplet impingement and breakup on a dry surface, *Comput. Fluids* 39 (9) (2010) 1696–1703.
- [71] J. Hyvälöuma, J. Timonen, Impact states and energy dissipation in bouncing and non-bouncing droplets, *J. Stat. Mech.: Theory Exp.* P06010 (2009) V.
- [72] A. Riaud, K. Wang, G. Luo, A combined lattice-Boltzmann method for the simulation of two-phase flows in microchannel, *Chem. Eng. Sci.* 99 (2013) 238–249.
- [73] W. Wang, Z. Liu, Y. Jin, Y. Cheng, LBM simulation of droplet formation in micro-channels, *Chem. Eng. J.* 173 (3) (2011) 828–836.
- [74] H. Yang, Q. Zhou, L.-S. Fan, Three-dimensional numerical study on droplet formation and cell encapsulation process in a micro T-junction, *Chem. Eng. Sci.* 87 (2013) 100–110.
- [75] S. Zhao, W. Wang, M. Zhang, T. Shao, Y. Jin, Y. Cheng, Three-dimensional simulation of mixing performance inside droplets in micro-channels by lattice Boltzmann method, *Chem. Eng. J.* 207–208 (2012) 267–277.
- [76] J. Cui, W. Li, W.-H. Lam, Numerical investigation on drag reduction with superhydrophobic surfaces by lattice-Boltzmann method, *Comput. Math. Appl.* 61 (12) (2011) 3678–3689.
- [77] B. Zhang, J. Wang, X. Zhang, Effects of the hierarchical structure of rough solid surfaces on the wetting of microdroplets, *Langmuir* 29 (22) (2013) 6652–6658.
- [78] N. Moradi, M. Gross, F. Varnik, G. Zikos, I. Steinbach, Morphologies of small droplets on patterned hydrophobic substrates, *Model. Simul. Mater. Sci. Eng.* 19 (2011) 045005.
- [79] X.-P. Chen, C.-W. Zhong, X.-L. Yuan, Lattice Boltzmann simulation of cavitating bubble growth with large density ratio, *Comput. Math. Appl.* 61 (12) (2011) 3577–3584.
- [80] P. Raiskinmäki, A. Shakib-Manesh, A. Jäsberg, A. Koponen, J. Merikoski, J. Timonen, Lattice-Boltzmann simulation of capillary rise dynamics, *J. Stat. Phys.* 107 (1–2) (2002) 143–158.
- [81] F.G. Wolf, L.O.E. dos Santos, P.C. Philippi, Capillary rise between parallel plates under dynamic conditions, *J. Colloid Interface Sci.* 344 (1) (2010) 171–179.
- [82] J. Hyvälöuma, P. Raiskinmäki, A. Jäsberg, A. Koponen, M. Kataja, J. Timonen, Evaluation of a lattice-Boltzmann method for mercury intrusion porosimetry simulations, *Future Gener. Comput. Syst.* 20 (2004) 1003–1011.

- [83] S. Chibbaro, L. Biferale, K. Binder, D. Dimitrov, F. Diotallevi, A. Milchev, S. Succi, Hydrokinetic simulations of nanoscopic precursor films in rough channels, *J. Stat. Mech.: Theory Exp.* P06007 (2009).
- [84] S. Chibbaro, Capillary filling with pseudo-potential binary lattice-Boltzmann model, *Eur. Phys. J. E* 27 (1) (2008) 99–106.
- [85] S. Chibbaro, L. Biferale, F. Diotallevi, S. Succi, K. Binder, D. Dimitrov, A. Milchev, S. Girardo, D. Pisignano, Evidence of thin-film precursors formation in hydrokinetic and atomistic simulations of nano-channel capillary filling, *EPL (Europhys. Lett.)* 84 (4) (2008) 44003.
- [86] P. Perlekar, L. Biferale, M. Sbragaglia, S. Srivastava, F. Toschi, Droplet size distribution in homogeneous isotropic turbulence, *Phys. Fluids* 24 (2012) 065101.
- [87] G. Falcucci, G. Chiatti, S. Succi, A.A. Mohamad, A. Kuzmin, Rupture of a ferrofluid droplet in external magnetic fields using a single-component lattice Boltzmann model for nonideal fluids, *Phys. Rev. E* 79 (5) (2009) 056706.
- [88] G. Falcucci, S. Succi, S. Ubertini, Magnetically driven droplet break-up and vaporization: a lattice Boltzmann study, *J. Stat. Mech: Theory Exp.* (2010) P05010.
- [89] A. Gupta, R. Kumar, Lattice Boltzmann simulation to study multiple bubble dynamics, *Int. J. Heat Mass Transfer* 51 (21–22) (2008) 5192–5203.
- [90] N.S. Martys, J.F. Douglas, Critical properties and phase separation in lattice Boltzmann fluid mixtures, *Phys. Rev. E* 63 (2001) 031205.
- [91] N. González-Segredo, M. Nekovee, P.V. Coveney, Three-dimensional lattice-Boltzmann simulations of critical spinodal decomposition in binary immiscible fluids, *Phys. Rev. E* 67 (4) (2003) 046304.
- [92] A.R. Imre, G. Mayer, G. Házi, R. Rozas, T. Kraska, Estimation of the liquid-vapor spinodal from interfacial properties obtained from molecular dynamics and lattice Boltzmann simulations, *J. Chem. Phys.* 128 (11) (2008) 114708.
- [93] H. Xi, C. Duncan, Lattice Boltzmann simulations of three-dimensional single droplet deformation and breakup under simple shear flow, *Phys. Rev. E* 59 (3) (1999) 3022–3026.
- [94] E. Monaco, G. Brenner, K. Luo, Numerical simulation of the collision of two microdroplets with a pseudopotential multiple-relaxation-time lattice Boltzmann model, *Microfluid Nanofluid* (2013) 1–18.
- [95] D. Lycett-Brown, I. Karlin, K.H. Luo, Droplet collision simulation by multi-speed lattice Boltzmann method, *Commun. Comput. Phys.* 9 (5) (2011) 1219–1234.
- [96] J. Harting, C. Kunert, J. Hyvaluoma, Lattice Boltzmann simulations in microfluidics: probing the no-slip boundary condition in hydrophobic, rough, and surface nanobubble laden microchannels, *Microfluid Nanofluid* 8 (2010) 1–10.
- [97] G. Tang, W.-Q. Tao, Y.-L. He, Lattice Boltzmann method for gaseous microflows using kinetic theory boundary conditions, *Phys. Fluids* 17 (2005) 058101.
- [98] X. Nie, G. Doolen, S. Chen, Lattice-Boltzmann simulations of fluid flows in MEMS, *J. Stat. Phys.* 107 (112) (2002) 279.
- [99] R. Benzi, L. Biferale, M. Sbragaglia, S. Succi, F. Toschi, Mesoscopic two-phase model for describing apparent slip in micro-channel flows, *EPL (Europhys. Lett.)* 74 (4) (2006) 651.
- [100] L. Zhu, D. Tretheway, L. Petzold, C. Meinhart, Simulation of fluid slip at 3D hydrophobic microchannel walls by the lattice Boltzmann method, *J. Comput. Phys.* 202 (1) (2005) 181–195.
- [101] J. Harting, C. Kunert, H.J. Herrmann, Lattice Boltzmann simulations of apparent slip in hydrophobic microchannels, *EPL (Europhys. Lett.)* 75 (2) (2006) 328.
- [102] C. Kunert, J. Harting, Roughness induced boundary slip in microchannel flows, *Phys. Rev. Lett.* 99 (17) (2007) 176001.
- [103] J. Hyväluoma, J. Harting, Slip flow over structured surfaces with entrapped microbubbles, *Phys. Rev. Lett.* 100 (24) (2008) 246001.
- [104] J. Hyväluoma, C. Kunert, J. Harting, Simulations of slip flow on nanobubble-laden surfaces, *J. Phys.: Condens. Matter* 23 (2011) 184106.
- [105] C. Pan, M. Hilpert, C.T. Miller, Lattice-Boltzmann simulation of two-phase flow in porous media, *Water Resour. Res.* 40 (1) (2004) W01501.
- [106] C. Pan, J.F. Prins, C.T. Miller, A high-performance lattice Boltzmann implementation to model flow in porous media, *Comput. Phys. Commun.* 158 (2) (2004) 89–105.
- [107] M.C. Sukop, D. Or, Lattice Boltzmann method for modeling liquid-vapor interface configurations in porous media, *Water Resour. Res.* 40 (2004) W01509.
- [108] J. Chin, E.S. Boek, P.V. Coveney, Lattice Boltzmann simulation of the flow of binary immiscible fluids with different viscosities using the Shan-Chen microscopic interaction model, *Philos. Trans. R. Soc. Lond. A* 360 (2002) 547–558.
- [109] B. Dong, Y.Y. Yan, W. Li, Y. Song, Lattice Boltzmann simulation of viscous fingering phenomenon of immiscible fluids displacement in a channel, *Comput. Fluids* 39 (2010) 768–779.
- [110] B. Dong, Y.Y. Yan, W.Z. Li, LBM simulation of viscous fingering phenomenon in immiscible displacement of two fluids in porous media, *Transp. Porous Media* 88 (2) (2011) 293–314.
- [111] P. Grosfils, J.P. Boon, J. Chin, E.S. Boek, Structural and dynamical characterization of Hele-Shaw viscous fingering, *Philos. Trans. R. Soc. Lond. A* 362 (2004) 1723–1734.
- [112] H. Li, C. Pan, C.T. Miller, Pore-scale investigation of viscous coupling effects for two-phase flow in porous media, *Phys. Rev. E* 72 (2005) 2005.
- [113] A. Ghassemi, A. Pak, Numerical study of factors influencing relative permeabilities of two immiscible fluids flowing through porous media using lattice Boltzmann method, *J. Petrol. Sci. Eng.* 77 (1) (2011) 135–145.
- [114] H. Huang, Z. Li, S. Liu, X.-Y. Lu, Shan-and-Chen-type multiphase lattice Boltzmann study of viscous coupling effects for two-phase flow in porous media, *Int. J. Numer. Methods Fluids* 61 (2009) 341–354.
- [115] H. Huang, X.-Y. Lu, Relative permeabilities and coupling effects in steady-state gas–liquid flow in porous media: a lattice Boltzmann study, *Phys. Fluids* 21 (2009) 092104.
- [116] Z. Dou, Z.-F. Zhou, Numerical study of non-uniqueness of the factors influencing relative permeability in heterogeneous porous media by lattice Boltzmann method, *Int. J. Heat Fluid Flow* 42 (2013) 23–32.
- [117] M.L. Porter, M.G. Schaap, D. Wildenschild, Lattice-Boltzmann simulations of the capillary pressure–saturation–interfacial area relationship for porous media, *Adv. Water Resour.* 32 (11) (2009) 1632–1640.
- [118] M. Zhang, G. Ye, K. van Breugel, Modeling of ionic diffusivity in non-saturated cement-based materials using lattice Boltzmann method, *Cem. Concr. Res.* 42 (11) (2012) 1524–1533.
- [119] L. Chen, H.-B. Luan, Y.-L. He, W.-Q. Tao, Numerical investigation of liquid water transport and distribution in porous gas diffusion layer of a proton exchange membrane fuel cell using lattice Boltzmann method, *Russ. J. Electrochim.* 48 (7) (2012) 712–726.
- [120] K. Jiao, X. Li, Water transport in polymer electrolyte membrane fuel cells, *Prog. Energy Combust. Sci.* 37 (221–291) (2011).
- [121] P.P. Mukherjee, Q. Kang, C.-Y. Wang, Pore-scale modeling of two-phase transport in polymer electrolyte fuel cells—progress and perspective, *Energy Environ. Sci.* 4 (2011) 346–369.
- [122] A.A. Shaha, K.H. Luo, T.R. Ralph, F.C. Walsha, Recent trends and developments in polymer electrolyte membrane fuel cell modelling, *Electrochim. Acta* 56 (2011) 3731–3757.
- [123] A. Arvay, E. Yli-Rantala, C.H. Liu, X.H. Peng, P. Koski, L. Cindrella, P. Kauranen, P.M. Wilde, A.M. Kannan, Characterization techniques for gas diffusion layers for proton exchange membrane fuel cells – a review, *J. Power Sources* 213 (2012) 317–337.
- [124] P.K. Sinha, P.P. Mukherjee, C.-Y. Wang, Impact of GDL structure and wettability on water management in polymer electrolyte fuel cells, *J. Mater. Chem.* 17 (2007) 3089–3103.
- [125] L. Chen, T.-F. Cao, Z.-H. Li, Y.-L. He, W.-Q. Tao, Numerical investigation of liquid water distribution in the cathode side of proton exchange membrane fuel cell and its effects on cell performance, *Int. J. Hydrogen Energy* 37 (11) (2012) 9155–9170.
- [126] T. Koido, T. Furusawa, K. Moriyama, An approach to modeling two-phase transport in the gas diffusion layer of a proton exchange membrane fuel cell, *J. Power Sources* 175 (1) (2008) 127–136.
- [127] J. Park, X. Li, Multi-phase micro-scale flow simulation in the electrodes of a PEM fuel cell by lattice Boltzmann method, *J. Power Sources* 178 (1) (2008) 248–257.
- [128] Y. Gao, X. Zhang, P. Rama, R. Chenc, H. Ostadi, K. Jiang, Lattice Boltzmann simulation of water and gas flow in porous gas diffusion layers in fuel cells reconstructed from micro-tomography, *Comput. Math. Appl.* 65 (2013) 891–900.
- [129] B. Han, H. Meng, Numerical studies of interfacial phenomena in liquid water transport in polymer electrolyte membrane fuel cells using the lattice Boltzmann method, *Int. J. Hydrogen Energy* 38 (12) (2013) 5053–5059.
- [130] L. Chen, H.-B. Luan, Y.-L. He, W.-Q. Tao, Pore-scale flow and mass transport in gas diffusion layer of proton exchange membrane fuel cell with interdigitated flow fields, *Int. J. Therm. Sci.* 51 (2012) 132–144.
- [131] S.G. Lee, D.H. Jeon, B.M. Kim, J.H. Kang, C.-J. Kim, Lattice Boltzmann simulation for electrolyte transport in porous electrode of lithium ion batteries, *J. Electrochim. Soc.* 160 (4) (2013) H258–H265.
- [132] B. Han, J. Yu, H. Meng, Lattice Boltzmann simulations of liquid droplets development and interaction in a gas channel of a proton exchange membrane fuel cell, *J. Power Sources* 202 (2012) 175–183.
- [133] B. Han, H. Meng, Lattice Boltzmann simulation of liquid water transport in turning regions of serpentine gas channels in proton exchange membrane fuel cells, *J. Power Sources* 217 (2012) 268–279.
- [134] Z.L. Yang, T.N. Dinh, R.R. Nourgaliev, B.R. Sehgal, Numerical investigation of bubble growth and detachment by the lattice-Boltzmann method, *Int. J. Heat Mass Transfer* 44 (1) (2001) 195–206.
- [135] A. Márkus, G. Házi, On the bubble departure diameter and release frequency based on numerical simulation results, *Int. J. Heat Mass Transfer* 52 (2009) 1472–1480.
- [136] A. Márkus, G. Házi, Numerical simulation of the detachment of bubbles from a rough surface at microscale level, *Nucl. Eng. Des.* 248 (2012) 263–269.
- [137] S. Gong, P. Cheng, Lattice Boltzmann simulation of periodic bubble nucleation, growth and departure from a heated surface in pool boiling, *Int. J. Heat Mass Transfer* 64 (2013) 122–132.
- [138] L. Biferale, P. Perlekar, M. Sbragaglia, F. Toschi, Convection in multiphase fluid flows using lattice Boltzmann methods, *Phys. Rev. Lett.* 108 (10) (2012) 104502.
- [139] X. Liu, P. Cheng, Lattice Boltzmann simulation of steady laminar film condensation on a vertical hydrophilic subcooled flat plate, *Int. J. Heat Mass Transfer* 62 (2013) 507–514.
- [140] X. Liu, P. Cheng, Lattice Boltzmann simulation for dropwise condensation of vapor along vertical hydrophobic flat plates, *Int. J. Heat Mass Transfer* 64 (2013) 1041–1052.

- [141] A.S. Joshi, Y. Sun, Multiphase lattice Boltzmann method for particle suspensions, *Phys. Rev. E* 79 (6) (2009) 066703.
- [142] A.S. Joshi, Y. Sun, Wetting dynamics and particle deposition for an evaporating colloidal drop: a lattice Boltzmann study, *Phys. Rev. E* 82 (4) (2010) 041401.
- [143] F. Jansen, J. Harting, From Bijels to Pickering emulsions: a lattice Boltzmann study, *Phys. Rev. E* 83 (2011) 046707.
- [144] S. Frijters, F. Günther, J. Harting, Effects of nanoparticles and surfactant on droplets in shear flow, *Soft Matter* 8 (2012) 6542–6556.
- [145] T. Krüger, S. Frijters, F. Günther, B. Kaoui, J. Harting, Numerical simulations of complex fluid–fluid interface dynamics, *Eur. Phys. J. Spec. Top.* 222 (1) (2013) 177–198.
- [146] X. Shi, H. Gaoa, V.I. Lazouskaya, Q. Kang, Y. Jin, L.-P. Wang, Viscous flow and colloid transport near air–water interface in a microchannel, *Comput. Math. Appl.* 59 (2010) 2290–2304.
- [147] A. Parmigiani, C. Huber, O. Bachmann, B. Chopard, Pore scale mass and reactant transport in multiphase porous media flows, *J. Fluid Mech.* 686 (2011) 40–76.
- [148] S.V. Lishchuk, C.M. Care, I. Halliday, Lattice Boltzmann algorithm for surface tension with greatly reduced microcurrents, *Phys. Rev. E* 67 (2003) 036701.
- [149] R. Benzi, L. Biferale, M. Sbragaglia, S. Succi, F. Toschi, Mesoscopic modeling of a two-phase flow in the presence of boundaries: the contact angle, *Phys. Rev. E* 74 (2) (2006) 021509.
- [150] L. Scarbolo, D. Molin, P. Perlekar, M. Sbragaglia, A. Soldati, F. Toschi, Unified framework for a side-by-side comparison of different multicomponent algorithms: lattice Boltzmann method vs. phase field model, *J. Comput. Phys.* 234 (2013) 263–279.
- [151] T. Lee, P.F. Fischer, Eliminating parasitic currents in the lattice Boltzmann equation method for nonideal gases, *Phys. Rev. E* 74 (2006) 046709.
- [152] M.L. Porter, E.T. Coon, Q. Kang, J.D. Moulton, J.W. Carey, Multicomponent interparticle-potential lattice Boltzmann model for fluids with large viscosity ratios, *Phys. Rev. E* 86 (3) (2012) 036701.